Electronic Supplementary Material (ESI) for Inorganic Chemistry Frontiers.

Supporting Information

Strong magnetic exchange coupling in Ln_2 metallocenes attained by the *trans*-coordination of a tetrazinyl radical ligand

Niki Mavragani,[a] Alexandros A. Kitos,[a] Jakub Hrubý,[b] Stephen Hill,[b,c] Akseli Mansikkamäki,[d] Jani O. Moilanen,[e] and Muralee Murugesu*[a]

Table of Contents:

1. Experimental Section	**S2**
2. IR Spectroscopy	**S3**
3. Single-crystal X-ray data and molecular features	**S3-S7**
4. Additional dc magnetic data for complexes 1-4	**S7-S9**
5. High-frequency electron paramagnetic resonance (HF-EPR) spectroscopy	**S9-S12**
6. Computational details and discussion	**S13-S34**
7. Additional ac magnetic data for complexes 1-3	**S34-S45**
8. References	**S46**

[a] *Department of Chemistry and Biomolecular Sciences, University of Ottawa, 10 Marie Curie, Ottawa, Ontario, K1N 6N5, Canada.*
[b] *National High Magnetic Field Laboratory, Florida State University, Tallahassee, Florida 32310, United States*
[c] *Department of Physics, Florida State University, Tallahassee, Florida 32306, United States.*
[d] *NMR Research Unit, University of Oulu, P.O. Box 300, 90014 Oulu, Finland.*
[e] *Department of Chemistry, Nanoscience Centre, University of Jyväskylä, P.O. Box 35, FI-40014, Finland.*
E-mail: m.murugesu@uottawa.ca

1. Experimental Section

General Procedures and Materials: All operations were performed in a Mbraun glovebox under an N_2 atmosphere. Solvents were dried using a J. C. Meyer solvent system, degassed by free-pump-thaw method and stored over activated 4 Å molecular sieves prior to use. The 3,6-bis(3,5-dimethyl-pyrazolyl)-1,2,4,5-tetrazine (bpytz) ligand was prepared according to the literature.[1] [Cp^*_2Ln][(μ-Ph_2)BPh_2] (Ln = Gd^{III}, Tb^{III}, Dy^{III}, Y^{III}) starting materials were prepared according to the literature.[2] All reagents were purchased from TCI, Alfa Aesar, or Strem Chemicals and used without further purification. HCp* (99+%) was purchased from Alfa Aesar and was degassed/dried as previously described prior to use. FT-IR spectra were recorded on a Nicolet Nexus 550 FT-IR spectrometer in the transmission window of 400-4000 cm^{-1}. Elemental Analysis was performed by Midwest Microlab. The X-band EPR spectrum of [$(Cp^*_2Y)_2$($bpytz^{\bullet-}$)][BPh_4] was recorded at ambient temperature using a Bruker EMX-200 spectrometer. The sample was dissolved in dry, degassed THF.

Synthesis of [$(Cp^*_2Gd)_2$($bpytz^{\bullet-}$)][BPh_4] (1): In 5 mL THF, one equivalent of bpytz (0.125 mmol, 33 mg) was combined with one equivalent of Cp_2Co (0.125 mmol, 24 mg) altering the colour of the ligand from red to green. The green slurry was added to a solution of two equivalents of [(Cp^*_2Gd][(μ-Ph_2)(BPh_2)] (0.25 mmol, 187mg) resulting in a dark purple solution. The reaction solution was left to stir for 2 hours and then filtrated. Upon slow diffusion with Et_2O, dark purple crystals of **1** were isolated after two days in 65% yield. Elemental Analysis: Complex **1** was analyzed as solvent free: Calcd: C, 63.17 %; H, 6.56 %; N, 7.76%, Found: C, 62.76%; H, 6.96%; N, 7.31%.

Synthesis of [$(Cp^*_2Tb)_2$($bpytz^{\bullet-}$)][BPh_4] (2), [$(Cp^*_2Dy)_2$($bpytz^{\bullet-}$)][BPh_4] (3) and [$(Cp^*_2Y)_2$($bpytz^{\bullet-}$)][BPh_4] (4):These complexes were prepared in a similar manner as **1** by simply replacing [Cp^*_2Gd][(μ-Ph_2)BPh_2] with [Cp^*_2Tb][(μ-Ph_2)BPh_2] (0.25 mmol, 187 mg) in **2**, [Cp^*_2Dy][(μ-Ph_2)BPh_2] (0.25 mmol, 188 mg) in **3** and [Cp^*_2Y][(μ-Ph_2)BPh_2] (0.25 mmol, 169 mg) in **4**. Yields = 64-67%. Elemental Analysis: Complex **2** was analyzed as solvent free: Calcd: C, 63.03%; H, 6.54%; N, 7.74%, Found: C, 62.89%; H, 6.35%; N, 7.14%. Complex **3** was analyzed as **3**·3THF: Calcd: C, 63.22%; H, 7.11%; N, 6.71 %, Found: C, 63.18 %; H, 6.97%; N, 7.04%. Elemental Analysis: Complex **4** was analyzed as solvent free: Calcd: C, 69.77 %; H, 7.24 %; N, 8.57 %, Found: C, 69.33 %; H, 7.39 %; N, 8.19 %.

Single Crystal X-ray Diffraction: Suitable crystals for single-crystal X-ray diffraction (SCXRD) analysis were covered in parabar oil and mounted on a thin glass fiber. Full data (Table S1) were collected on a Bruker KAPPA APEX-II CCD single-crystal diffractometer (graphite monochromated Mo-Kα radiation, λ = 0.71073 Å), at 213 K temperature. Absorption corrections were applied by using multi-scan of the SADABS[3] program. Structures were solved using direct methods with SHELXT[4] and refined by the full-matrix least-squares methods on F^2 with SHELXL-2018/3[5] in anisotropic approximation for all non-hydrogen atoms. Carbon-bound hydrogen atoms were included in calculated positions (see details in the CIF files). The crystal structures of **1**, **2**, **3** and **4** contain an area of highly disordered solvent molecules (mostly diethyl ether and tetrahydrofuran molecules with partial occupancies) resulting in a smeared-out electron density. Attempts to model the disordered areas with chemically and crystallographic reasonable geometries were unsuccessful. Therefore, the SQUEEZE[6] function of PLATON[7] was used to remove the contribution of the electron density associated with those molecules from the intensity data. The crystal structures exhibited inversion twinning with domain ratios of 62:38 for **1**, 71:29 for **2**, 53:47 for **3** and 55:45 for **4** (see details in the CIF files). All geometric/crystallographic calculations were carried out using WINGX[8] package while the molecular/packing graphics were prepared with DIAMOND[9] and MERCURY.[10]

Magnetic Measurements: Magnetic susceptibility measurements were obtained using a Quantum Design SQUID magnetometer MPMS-XL7 operating between 1.8 and 300 K. Direct current (dc) measurements were performed on 22.0 mg (**1**), 19.8 mg (**2**), 22.0 mg (**3**) and 68.4 mg (**4**) of crushed polycrystalline samples, which were restrained with silicon grease and sealed in a polyethylene membrane, under an inert atmosphere, for which diamagnetic corrections were applied. The samples were subjected to dc fields of 70 to -70 kOe while alternating current (ac) measurements took place in the absence and presence of a static dc field (H_{dc} = 1400 Oe).

2. IR Spectroscopy

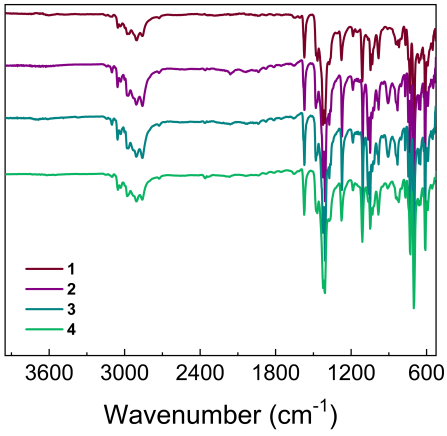

Fig. S1: Solid-state infrared (IR) spectra of complexes **1** (magenta), **2** (purple), **3** (blue) and **4** (teal).

3. Single-crystal X-ray data and molecular features

Table S1. Crystallographic data and refinement details for **1**, **2**, **3** and **4**.

Compound reference	1	2	3	4
Chemical formula	$C_{76}H_{94}BGd_2N_8$	$C_{76}H_{94}BN_8Tb_2$	$C_{76}H_{94}BDy_2N_8$	$C_{76}H_{94}BN_8Y_2$
Formula mass	1444.90	1448.24	1455.40	1308.22
Crystal system	Orthorhombic	Orthorhombic	Orthorhombic	Orthorhombic
a/Å	33.784(3)	33.7796(8)	33.8626(15)	33.8743(14)
b/Å	17.6753(13)	17.5822(4)	17.5484(8)	17.5163(7)
c/Å	13.0356(10)	13.0110(3)	12.9964(6)	12.9964(6)
$\alpha = \beta = \gamma$/°	90	90	90	90
Unit cell volume/Å^3	7784.0(10)	7727.5(3)	7722.9(6)	7711.4(6)
Temperature/K	213(2)	213(2)	213(2)	213(2)
Space group	$Pna2_1$	$Pna2_1$	$Pna2_1$	$Pna2_1$
No. of formula units/unit cell, *Z*	4	4	4	4
Radiation type	Mo Kα	Mo Kα	Mo Kα	Mo Kα
Absorption coefficient, μ/mm^{-1}	1.732	1.858	1.963	1.540
No. of reflections measured	59706	61262	68035	67495
No. of independent reflections	14705	14077	16464	13057
Data / parameters / restraints	14705 / 694 / 271	14077 / 809 / 97	16464 /809 / 409	13057 /808 / 25
R_{int}	0.0477	0.0460	0.0696	0.1091
Final R_1 values (all data)	0.0723	0.0534	0.0909	0.1140
Final $wR_2(F^2)$ values (all data)	0.1628	0.0916	0.1629	0.1793
Final R_1 values ($I > 2\sigma(I)$)	0.0637	0.0436	0.0667	0.0678
Final $wR_2(F^2)$ values ($I > 2\sigma(I)$)	0.1564	0.0882	0.1502	0.1618
Goodness of fit on F^2	1.090	1.162	1.096	1.016
Largest diff. peak and hole (eÅ^{-3})	3.487 / -2.306	1.599 / -1.339	2.819 / -3.287	1.444 / -1.081
CCDC number	2158048	2158049	2158050	2158051

Table S2. Selected distances (Å) and angles (º) for **1**, **2**, **3** and **4**.

	Distance/angle		Distance/angle
	1		
Gd1-Gd2$_{intra}$	7.584(10)	Gd1-Gd2$_{inter}$	8.846(10)
Gd1-N1$_{pyrazole}$	2.427(14)	Gd2-N5$_{tetrazine}$	2.435(11)
Gd1-N3$_{tetrazine}$	2.409(12)	Gd2-N8$_{pyrazole}$	2.444(12)
Gd1- Cp$_{cent}$*A	2.445(6)	Gd2-Cp$_{cent}$*C	2.435(6)
Gd1-Cp$_{cent}$*B	2.433(6)	Gd2-Cp$_{cent}$*D	2.439(6)
Gd1-bpytz$_{cent}$	3.782(7)	Gd2-bpytz$_{cent}$	3.804(7)
N3-N4	1.390(16)	N5-N6	1.384(15)
Cp$_{cent}$*A-Gd1-Cp$_{cent}$*B	141.98(24)	Cp$_{cent}$*C-Gd2-Cp$_{cent}$*D	141.15(24)
N1-Gd1-N3	64.89(44)	N5-Gd2-N8	65.02(36)
N1-Gd1-Cp$_{cent}$*A	106.99(26)	N5-Gd2-Cp$_{cent}$*C	105.52(25)
N1-Gd1-Cp$_{cent}$*B	105.98(27)	N5-Gd2-Cp$_{cent}$*D	106.59(25)
N3-Gd1-Cp$_{cent}$*A	105.41(22)	N8-Gd2-Cp$_{cent}$*C	107.04(26)
N3-Gd1-Cp$_{cent}$*B	105.35(23)	N8-Gd2-Cp$_{cent}$*D	105.99(26)
	2		
Tb1-Tb2$_{intra}$	7.568(8)	Tb1-Tb2$_{inter}$	8.796(5)
Tb1-N1$_{pyrazole}$	2.436(8)	Tb2-N5$_{tetrazine}$	2.399(8)
Tb1-N3$_{tetrazine}$	2.432(7)	Tb2-N8$_{pyrazole}$	2.406(8)
Tb1- Cp$_{cent}$*A	2.376(9)	Tb2-Cp$_{cent}$*C	2.381(10)
Tb1-Cp$_{cent}$*B	2.368(9)	Tb2-Cp$_{cent}$*D	2.377(9)
Tb1-bpytz$_{cent}$	3.797(7)	Tb2-bpytz$_{cent}$	3.773(6)
N3-N4	1.385(10)	N5-N6	1.388(10)
Cp$_{cent}$*A-Tb1-Cp$_{cent}$*B	141.46(14)	Cp$_{cent}$*C-Tb2-Cp$_{cent}$*D	141.76(14)
N1-Tb1-N3	65.19(20)	N5-Tb2-N8	65.34(20)
N1-Tb1-Cp$_{cent}$*A	106.83(22)	N5-Tb2-Cp$_{cent}$*C	105.75(23)
N1-Tb1-Cp$_{cent}$*B	106.14(22)	N5-Tb2-Cp$_{cent}$*D	105.51(23)
N3-Tb1-Cp$_{cent}$*A	105.42(20)	N8-Tb2-Cp$_{cent}$*C	106.85(22)
N3-Tb1-Cp$_{cent}$*B	106.16(22)	N8-Tb2-Cp$_{cent}$*D	105.88(23)
	3		
Dy1-Dy2$_{intra}$	7.548(9)	Dy1-Dy2$_{inter}$	8.908(8)
Dy1-N1$_{pyrazole}$	2.423(13)	Dy2-N5$_{tetrazine}$	2.402(12)
Dy1-N3$_{tetrazine}$	2.419(12)	Dy2-N8$_{pyrazole}$	2.395(13)
Dy1- Cp$_{cent}$*A	2.357(6)	Dy2-Cp$_{cent}$*C	2.369(5)
Dy1-Cp$_{cent}$*B	2.356(5)	Dy2-Cp$_{cent}$*D	2.377(5)
Dy1-bpytz$_{cent}$	3.786(6)	Dy2-bpytz$_{cent}$	3.764(6)
N3-N4	1.397(16)	N5-N6	1.379(17)
Cp$_{cent}$*A- Dy1-Cp$_{cent}$*B	141.44(24)	Cp$_{cent}$*C- Dy2-Cp$_{cent}$*D	141.59(24)
N1- Dy1-N3	65.41(40)	N5- Dy2-N8	66.20(42)
N1- Dy1-Cp$_{cent}$*A	105.98(30)	N5- Dy2-Cp$_{cent}$*C	105.80(26)
N1- Dy1-Cp$_{cent}$*B	106.71(30)	N5- Dy2-Cp$_{cent}$*D	105.34(26)
N3- Dy1-Cp$_{cent}$*A	106.38(26)	N8- Dy2-Cp$_{cent}$*C	106.10(27)
N3- Dy1-Cp$_{cent}$*B	105.44(26)	N8- Dy2-Cp$_{cent}$*D	106.70(26)
	4		
Y1- Y2$_{intra}$	7.527(11)	Y1- Y2$_{inter}$	8.765(11)
Y1-N1$_{pyrazole}$	2.397(7)	Y2-N6$_{tetrazine}$	2.382(7)
Y1-N3$_{tetrazine}$	2.394(7)	Y2-N8$_{pyrazole}$	2.391(8)
Y1- Cp$_{cent}$*A	2.348(7)	Y2-Cp$_{cent}$*C	2.349(7)
Y1-Cp$_{cent}$*B	2.354(7)	Y2-Cp$_{cent}$*D	2.365(7)
Y1-bpytz$_{cent}$	3.772(7)	Y2-bpytz$_{cent}$	3.757(7)

N3-N4	1.414(10)	N5-N6	1.403(10)
Cp_{cent}*A- Y1-Cp_{cent}*B	140.12(32)	Cp_{cent}*C- Y2-Cp_{cent}*D	141.76(32)
N1- Y1-N3	65.96(22)	N6- Y2-N8	64.88(26)
N1- Y1-Cp_{cent}*A	106.98(14)	N6- Y2-Cp_{cent}*C	105.53(14)
N1- Y1-Cp_{cent}*B	106.94(14)	N6- Y2-Cp_{cent}*D	105.54(14)
N3- Y1-Cp_{cent}*A	106.66(14)	N8- Y2-Cp_{cent}*C	106.64(18)
N3- Y1-Cp_{cent}*B	105.88(14)	N8- Y2-Cp_{cent}*D	106.41(17)

Cp_{cent}*A: C13-C17, Cp_{cent}*B: C23-C27, Cp_{cent}*C: C33-C37, Cp_{cent}*D: C43-C47

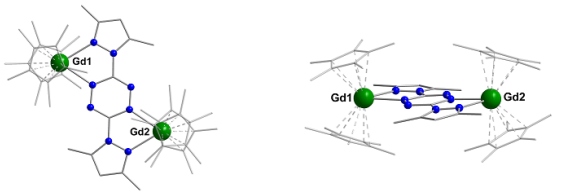

$[(Cp^*_2Gd^{III})_2(bpytz^{\bullet-})][BPh_4]$

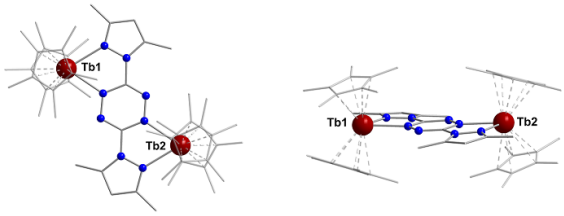

$[(Cp^*_2Tb^{III})_2(bpytz^{\bullet-})][BPh_4]$

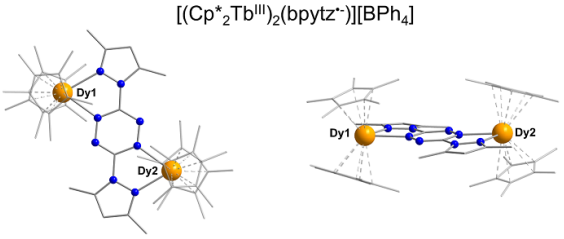

$[(Cp^*_2Dy^{III})_2(bpytz^{\bullet-})][BPh_4]$

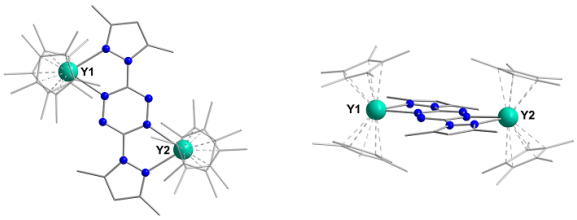

$[(Cp^*_2Y^{III})_2(bpytz^{\bullet-})][BPh_4]$

Fig. S2: Molecular structures of **1** (top), **2** (middle), **3** (middle) and **4** (bottom). For clarity reasons BPh_4^- moieties as well as H-atoms have been omitted.

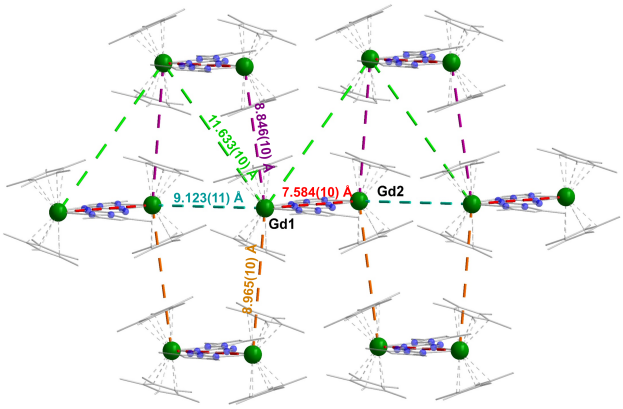

$[(Cp^*_2Gd^{III})_2(bpytz^{\bullet-})][BPh_4]$

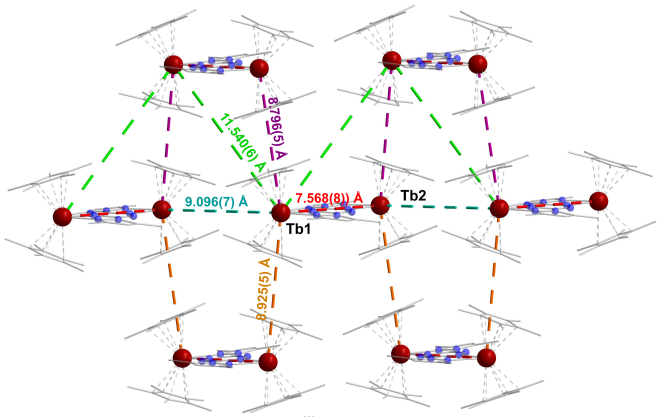

$[(Cp^*_2Tb^{III})_2(bpytz^{\bullet-})][BPh_4]$

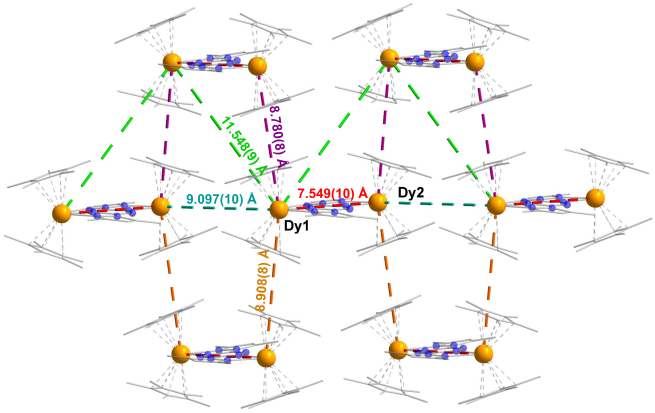

$[(Cp^*_2Dy^{III})_2(bpytz^{\bullet-})][BPh_4]$

Fig. S3: Intramolecular and intermolecular Ln···Ln distances for **1** (top), **2** (middle) and **3** (bottom). For clarity reasons, partial transparency has been employed and BPh_4^- as well as H-atoms have been omitted. Each Ln···Ln distance is colour coded.

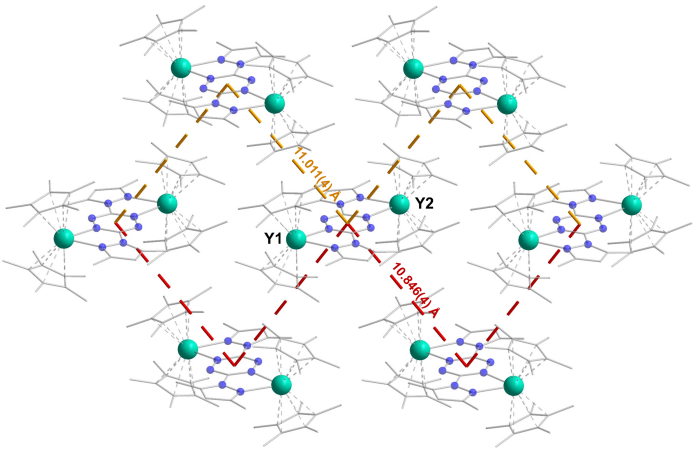

$[(Cp^*_2Y^{III})_2(bpytz^{\bullet-})][BPh_4]$

Fig. S4: Intermolecular $bpytz^{\bullet-}{}_{cent}\cdots bpytz^{\bullet-}{}_{cent}$ distances for **4**. For clarity reasons, partial transparency has been employed and BPh_4^- as well as H-atoms have been omitted. Each distance is colour coded.

4. Additional dc magnetic data for complexes 1-4:

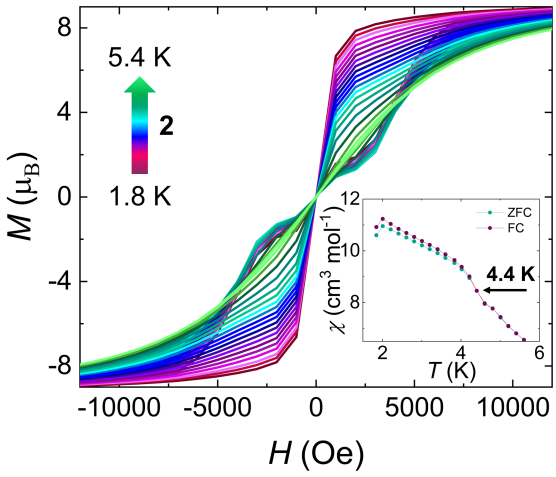

Fig. S5: Hysteresis sweep for **2**, from 1.8 to 5.4 K in the field range of 70 kOe to -70 kOe, with an average sweep rate of 31 Oe/s. Inset: Zero-field-cooled and field-cooled (ZFC/FC) curves for **2** under an applied static field of 1000 Oe. Data were collected at an average sweep rate of 0.14 K/min. The black arrow indicates ZFC and FC susceptibilities bifurcate at 4.4 K for **2**.

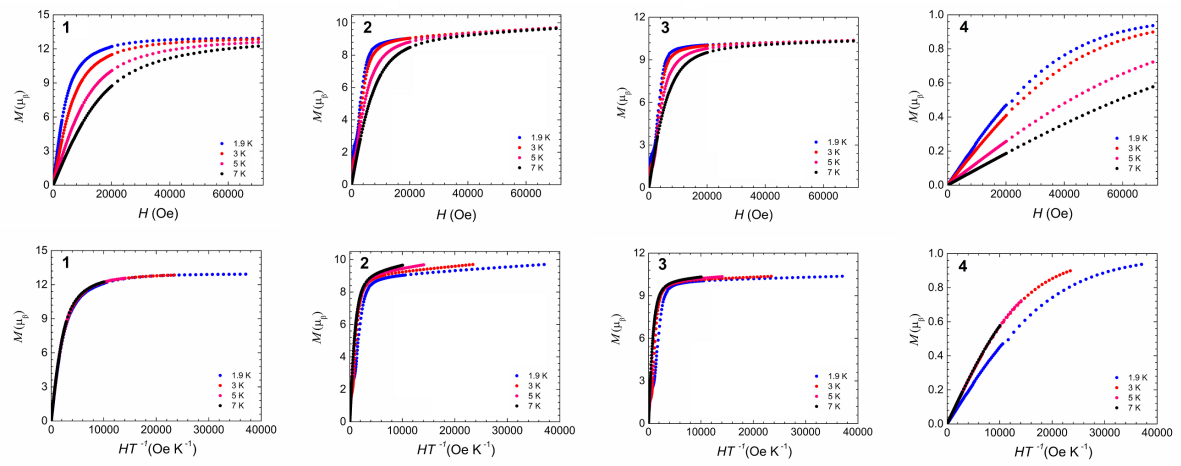

Fig. S6: Field dependence of the magnetization (top) and the reduced magnetization (bottom) for **1**-**4** at the indicated temperatures.

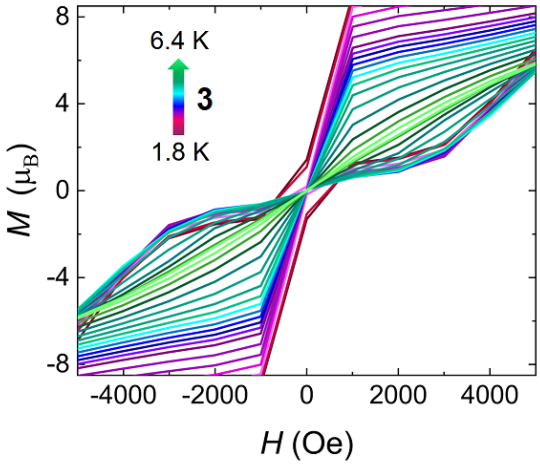

Fig. S7: Hysteresis sweep for **3**, from 1.8 to 6.4 K in the field range of 70 kOe to -70 kOe, with an average sweep rate of 31 Oe/s. The figure represents a zoomed-in area, highlighting the opening of the loops at 1.8 and 2 K, and the crossing of the magnetization when $T \geq 2.4$ K.

Fit of the dc susceptibility data for 4:

The χT plot of **4** was fit using PHI software[11] to the below spin Hamiltonian, were zJ is the intermolecular interaction parameter:

$$\chi = \frac{\chi_0}{\frac{2zJ}{Ng^2\mu_B{}^2\chi_0}}$$

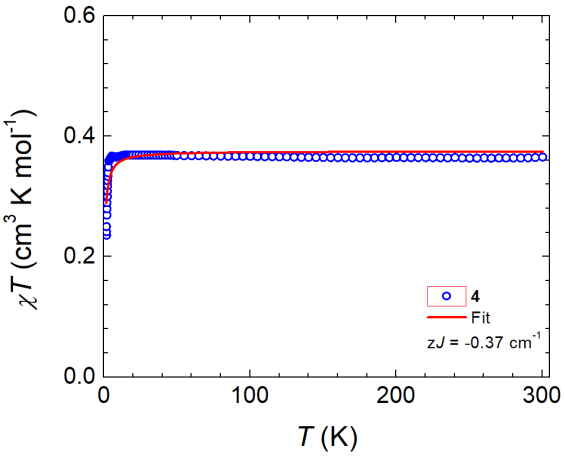

Fig. S8: Variable temperature dc susceptibility of **4** (blue circles) under an applied field of 1000 Oe.

5. High-frequency electron paramagnetic resonance (HF-EPR) spectroscopy

High-frequency electron paramagnetic resonance (HF-EPR) spectra were collected using a home-built spectrometer operating in continuous-wave mode at 240 GHz (cw-240 GHz), as described in detail previously.[12,13] All samples were measured as ground polycrystalline powders and mounted in an inert atmosphere EPR sample holder. All spectra were simulated using the EasySpin (version 6.0.0-dev.44) toolbox for Matlab.[14]

HF-EPR spectra were collected for **1**, **3**, and **4**. No EPR signal was observed for **3**, which is most likely due to the fact that it is an excellent single-molecule magnet (SMM) with little or no mixing between the low-energy spin-up and down states (m_S = ±S), such that the magnetic dipole transition matrix element between them is vanishingly small.

The Hamiltonian used for simulation of the spectra for the spin = ½ radical of complex **4** (Fig. S9) includes only the Zeeman contribution:

$$\widehat{H} = \mu_B \boldsymbol{B}_0 \cdot \tilde{\boldsymbol{g}} \cdot \widehat{\boldsymbol{S}},$$

where μ_B is Bohr magneton, $\boldsymbol{B}_0$ the externally applied magnetic field, $\tilde{\boldsymbol{g}}$ the Landé-tensor, and $\widehat{\boldsymbol{S}}$ is the spin angular momentum operator. The best simulation was obtained with the following parameters: $g_x = g_y = 2.0024 \pm 0.0002$, and $g_z = 2.0005 \pm 0.0002$. The nitrogen hyperfine structures seen in low-field spectra (Fig. 3D) are not resolved at high-fields due to the increased effect of g-strain broadening.

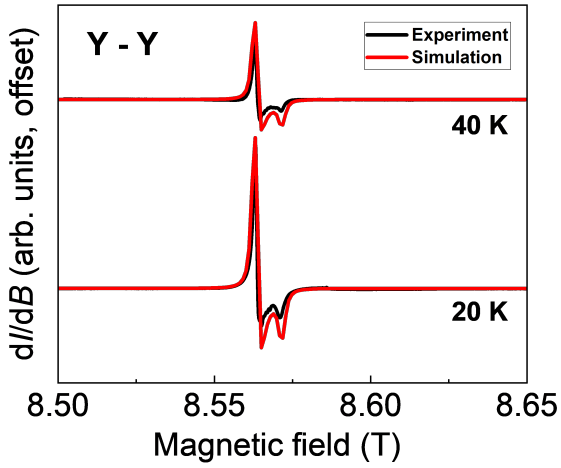

Fig. S9: Experimental Cw-240 GHz spectra (black) and simulations (red) for **4** at 20 and 40 K, revealing weak *g*-tensor anisotropy.

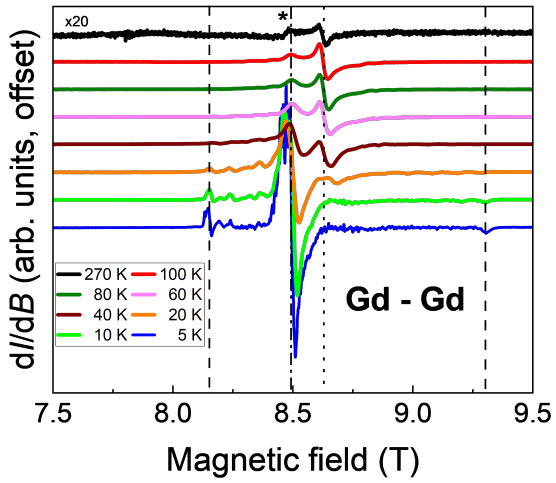

Fig. S10: Temperature dependent spectra for **1,** recorded at cw-240 GHz and 5, 10, 20, 40, 60, 80, 100, 270 K (see legend). The spectral features span from ~8.15 to ~9.3 T (dashed vertical lines), corresponding to effective *g*-values, g^{eff} = 2.10 and 1.84, respectively. The asterisk (*) denotes an impurity signal.

Fig. S10 displays variable temperature cw-240 GHz spectra for **1**. At the lowest temperature of 5 K, anisotropic contributions from the presumed ground $S = {}^{13}/_{2}$ state are clearly visible at the extremes of the spectrum (vertical dashed lines). Some of the sharp features and the apparent increase in noise at 5 K are due to finite-crystallite effects,[15,16] i.e., larger microcrystals within the powder that are randomly oriented, thus giving rise to ground-state signals in between the extremes of the powder spectrum (these broaden and wash-out at higher temperatures). The strong low-temperature signal at 8.5 T (g^{eff} = 2.015, dot-dash line in Fig. S10) is of unknown origin; possibilities include uncoupled Gd species with little or no zero-field splitting, or some other paramagnetic contaminant. Upon increasing the temperature, higher lying states within the $S = {}^{13}/_{2}$ manifold become thermally populated, as seen clearly at 20 K where evenly spaced features appear on either side of the 8.5 T signal (see also Fig. S11). At the highest temperatures, only the residual impurity signal and the central $S = {}^{13}/_{2}$, m_S = -½ to ½ transition (at 8.625 T or g^{eff} = 1.99, dotted vertical line in Fig. S10) persist; the latter has, by far, the strongest matrix element and experiences no first-order spin-orbit anisotropy, which broadens features in the wings of the spectrum.

Two different models were considered for simulation of the EPR spectra for compound **1**: (i) an effective giant spin Hamiltonian (GSH) approach, which was then compared to (ii) a multi-spin Hamiltonian (MSH) analysis. The former is often used for polynuclear systems[17] to save computational resources and minimize the number of adjustable parameters. However, the GSH formalism omits important microscopic details captured in the MSH approach, such as the nature of the coupling between the constituent spins.[18] The GSH model consists of Zeeman and zero-field splitting (ZFS) contributions:

$$\widehat{H} = \mu_{\mathrm{B}} \boldsymbol{B}_0 \cdot \tilde{\boldsymbol{g}} \cdot \widehat{\boldsymbol{S}} + D\hat{S}_z^2 + E\left(\hat{S}_x^2 - \hat{S}_y^2\right),$$

where the $\hat{S}_i$ $(i = x, y, z)$ denote components of the total spin operator, $\widehat{\boldsymbol{S}}$, with *D* and *E* respectively parameterizing the axial and rhombic 2nd-order ZFS interactions. The best simulations assume an *S* = $^{13}/_2$ ground state and GSA Hamiltonian parameters: $g_x = g_y = 1.987 \pm 0.002$, $g_z = 1.974 \pm 0.002$, $D = +0.047$ cm^{-1}, $E = +0.009$ cm^{-1}, with $E/D = 0.19$.

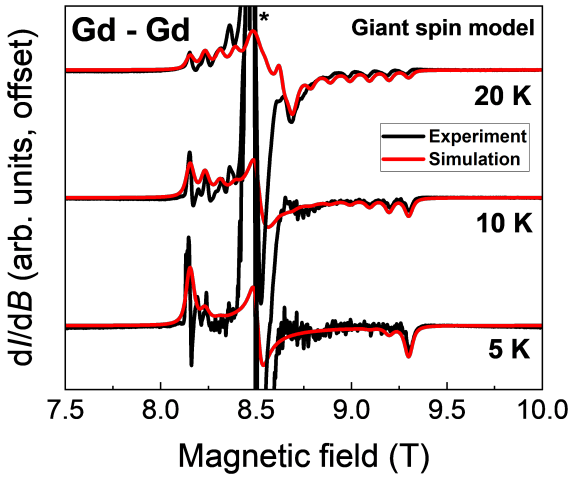

Fig. S11: Simulations (red) of the experimental cw-240 GHz spectra (black) using the GSA for temperatures of 5, 10, and 20 K.

The MSH simulations for **1** consisted of two Gd^{III} ions ($s = {}^7/_2$) bridged by the organic bpytz$^{\bullet-}$ radical ($s = {}^1/_2$); lowercase symbols are employed here to differentiate the parameters and operators associated with the individual spins from those of the GSA. The MSH is as follows:

$$\widehat{H} = \sum_i \left[\mu_B \boldsymbol{B}_0 \cdot \tilde{\boldsymbol{g}}_i \cdot \hat{\boldsymbol{s}}_i + d_i \hat{s}_{zi}^2 + e_i\left(\hat{s}_{xi}^2 - \hat{s}_{yi}^2\right)\right] - 2\sum_{i \neq j} J_{ij} \hat{\boldsymbol{s}}_i \cdot \hat{\boldsymbol{s}}_j.$$

The labels 1 and 3 represent the outer Gd^{III} ions with $s = {}^7/_2$, while label 2 denotes the $s = ½$ radical. Considering the two Gd^{III} sites identical, $\tilde{\boldsymbol{g}}_1 = \tilde{\boldsymbol{g}}_3 = \tilde{\boldsymbol{g}}_{\mathrm{Gd}}$; likewise, the ZFS parameters $d_1 = d_3 = d_{\mathrm{Gd}}$ and $e_1 = e_3 = e_{\mathrm{Gd}}$. Meanwhile, $\tilde{\boldsymbol{g}}_2 = \tilde{\boldsymbol{g}}_{\mathrm{rad}}$ and $d_2 = e_2 = 0$, as required for a spin = ½. The last term parameterizes the exchange interactions between the spins; note that the $-2JS_i \cdot S_j$ convention is used here. Again, following the same assumption for the two Gd^{III} sites as above, $J_{12} = J_{23} = J_{\mathrm{Gd-rad}}$, and we neglect the Gd-Gd exchange interaction (J_{13}) in our analysis as it is weak in comparison to $J_{\mathrm{Gd-rad}}$ (see below); indeed the small ferromagnetic Gd-Gd interaction deduced from fits to magnetic data had no effect on the EPR simulations.

Fig. S12 displays various simulations of the cw-240 GHz spectra using the MSH model. The best simulations were obtained assuming a strongly exchange-coupled ground state. To illustrate this point, Fig. S12a employs the antiferromagnetic Gd-rad coupling parameter, $J_{\mathrm{Gd-rad}} = -14$ cm^{-1}, deduced from magnetic fits. Such an interaction gives rise to a well-isolated total spin *S* = $^{13}/_2$ ground state. Therefore, it is not surprising that the best MSH simulations in Fig. S12a are very similar to those in Fig. S11. The corresponding single-spin *g*-tensors and ZFS parameters used for these simulations are: $g_{\mathrm{Gd},x} = g_{\mathrm{Gd},y} = 1.990$, $g_{\mathrm{Gd},z} = 1.968$, $g_{\mathrm{rad},x} = g_{\mathrm{rad},y} = 2.0024$, $g_{\mathrm{rad},z} = 2.0005$ (*g*-values for the radical were assumed to be the same as those for compound **4**), $d_{\mathrm{Gd}} = +0.0850 \pm 0.0007$ cm^{-1}, $e_{\mathrm{Gd}} = +0.0190 \pm 0.0007$ cm^{-1}, with $e_{\mathrm{Gd}}/d_{\mathrm{Gd}} = 0.22$. However, the simulations are insensitive to the value of $J_{\mathrm{Gd-rad}}$ so long as it is large in comparison to the ZFS parameters, i.e., so long as the *S* = $^{13}/_2$ ground state is well isolated from excited spin multiplets. As a sanity check, simulations were also performed in the weak exchange limit by setting $J_{\mathrm{Gd-rad}} = 0$, so that the molecule consists of two uncoupled $s = {}^7/_2$ Gd^{III} ions and an $s = ½$ radical (Fig. S12b). In this case, it is impossible to reproduce the spacing of the resonances in the wings of the spectra, because the maximum spin multiplicity ($2s + 1 = 8$) is too small, i.e., there are not enough resonances. As such, these measurements do confirm the results of the magnetic fits – namely that **1** has a strongly coupled giant spin ground state. We also performed simulations assuming a strong ferromagnetic exchange parameter, $J_{\mathrm{Gd-rad}} = +14$ cm^{-1} (Fig. S12c), which would give rise to a spin = $^{15}/_2$ ground state. By slightly adjusting the axial ZFS parameter, $d_{\mathrm{Gd}} = +0.0984 \pm 0.0007$ cm^{-1}, it was found that simulations of comparable quality to Fig. S12a could be obtained. As such, one sees that the HF-EPR spectra are able to confirm that the coupling is strong but cannot distinguish the small difference in total spin between the ferro- ($S = {}^{15}/_2$) and antiferromagnetic cases ($S = {}^{13}/_2$). By contrast, the fits to magnetic data can distinguish these two cases relatively easily. However, they are insensitive to the ZFS interactions associated with the Gd^{III} ions, so one sees here the complementarity of the two techniques.

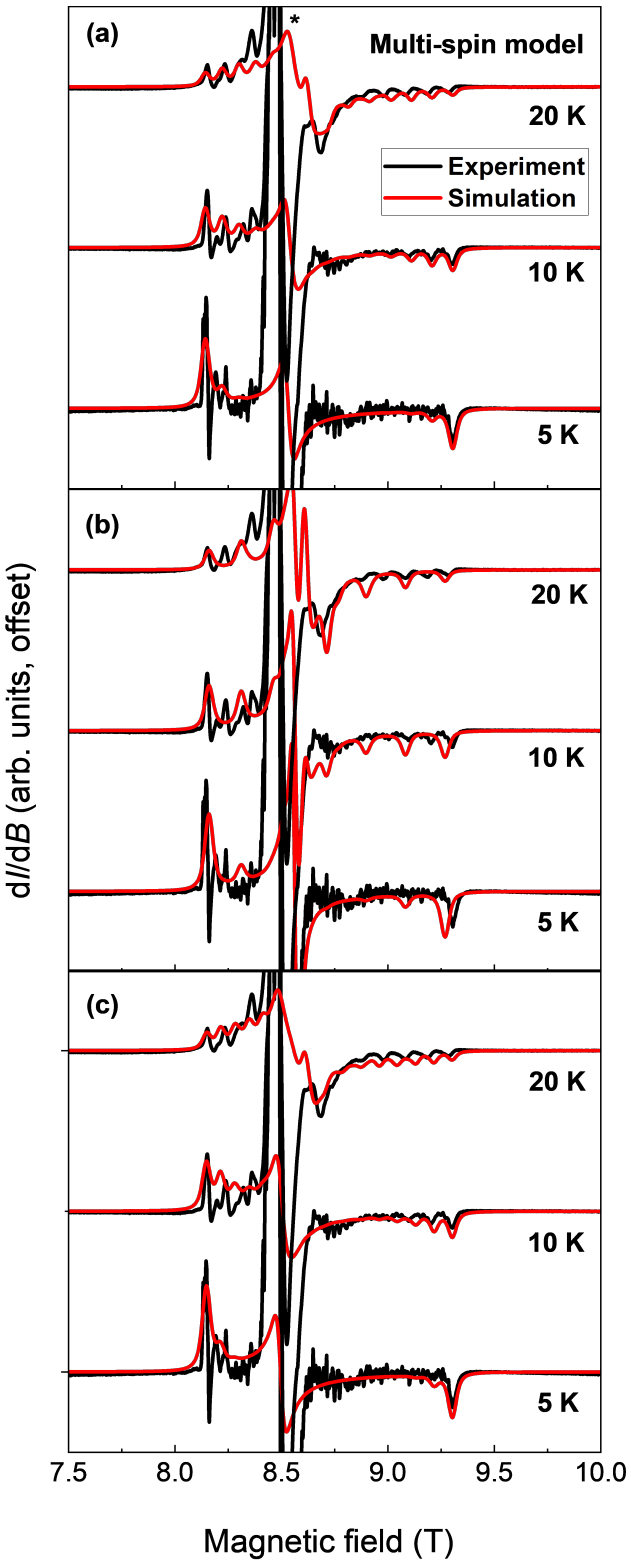

Fig. S12: Simulations of the cw-240 GHz HF-EPR spectra for **1** at 5, 10, and 20 K, for three different exchange coupling scenarios: (a) $J_{\mathrm{Gd-rad}} = -14$ cm^{-1}; (b) $J_{\mathrm{Gd-rad}} = 0$; and (c) $J_{\mathrm{Gd-rad}} = +14$ cm^{-1}. The asterisk denotes an impurity signal.

6. Computational details and discussion

The state-averaged complete active space self-consistent field (SA-CASSCF)[19] calculations were performed for each inequivalent Ln^{III} ions in **2** and **3** using the OpenMolcas quantum chemistry software version 20.11.[20] Prior to the SA-CASSCF calculations, the positions of the hydrogen atoms were optimized at the density functional (DFT) level of theory using the same procedure as described for **4** (see below). Two sets of SA-CASSCF calculations were carried out for each Ln^{III} center to extract the average crystal field parameters for **2** and **3** using the previously reported methodology.[21] In all calculations, the other Ln^{III} was replaced with an Y^{III} ion, whereas the $bpytz^{\bullet-}$ ligand was treated either as a neutral ligand (minus one electron) or a double anion (plus one electron) instead of the radical mono anion. In other words, the $bpytz^{\bullet-}$ ligand was described as a closed shell species in all SA-CASSCF calculations. For Dy^{III}, the active space consisted of nine 4f electrons and seven 4f orbitals, whereas for Tb^{III}, the active space consisted of eight 4f electrons and seven 4f orbitals. All 21 sextets, 224 quartets and 490 doublets were solved for Dy^{III} in the SA-CASSCF calculations, whereas for Tb^{III}, all 7 septets and 140 pentets were solved. Out of these states, all 21 sextet states, the lowest 128 quartets and lowest 130 doublets for Dy^{III} and all 7 septets and 140 pentets for Tb^{III} were mixed by spin-orbit coupling in the subsequent spin-orbit restricted active space interaction (SO-RASSI)[22] calculations. In all *ab initio* calculations scalar relativistic effects were taken into account using the exact two-component (X2C) transformation,[23] and the Cholesky decomposition of two-electron integrals with a threshold value of 10^{-8} (in atomic units) was used to speed up the calculations. Roos' relativistically contracted atomic natural orbital (ANO-RCC) basis sets with a valence-polarized triple-ζ-quality (VTZP) was used for Dy^{III} and Tb^{III} ions and valence-polarized double-ζ-quality (VDZP) for all other atoms.[24] Finally, the *ab initio* crystal field parameters were calculated using the SINGLE_ANISO[25] module for all investigated Ln^{III} ions. The averaged crystal field parameters were derived for each Ln^{III} center using the previously reported approach from the *ab initio* crystal field parameters.[21]

Simulation of low-lying exchange energy levels of **2** and **3** were carried out in a qualitive manner with the *PHI*[11] software (version 3.1.5) using the following Hamiltonian that takes into account the Ln–$bpytz^{\bullet-}$ exchange interaction and Zeeman splitting:

$$\widehat{H} = -\boldsymbol{J}_{rad-Ln}\left(\tilde{S}_{z,Ln1}\tilde{S}_{z,rad} + \tilde{S}_{z,Ln2}\tilde{S}_{z,rad}\right) + \mu_B B g_{zz}\tilde{S}_{z,Ln1} + \mu_B B g_{zz}\tilde{S}_{z,Ln2} + \mu_B B g_e \tilde{S}_{z,rad},$$

where $\boldsymbol{J}_{rad-Ln}$, $\tilde{S}_{z,Ln}$, $\tilde{S}_{z,rad}$, μ_B, B, g_{zz}, and g_e are an exchange coupling constant for Ln–$bpytz^{\bullet-}$ radical coupling, a pseudospin operator acting on the ground doublet of Ln^{III} ion, spin operator acting on the spin of the radical ligand, the Bohr magneton, the scalar magnitude of the external magnetic field, principal z component of the **g** tensor, and g-factor of the isotropic radical spin, respectively. Thus, the model was constructed on a basis of two pseudospin doublets describing the ground KDs of Dy^{III} ion or the ground pseudo doublets of Tb^{III} ion and one isotropic effective spin doublet describing the unpaired electron of $bpytz^{\bullet-}$ ligand. The Ln–$bpytz^{\bullet-}$exchange interaction was described within the Lines model[26] assuming a purely Ising type interaction. The assumption is valid because the angle between the main magnetic axes of Ln^{III} ions is 4.5° and 0° in **2** and **3**, respectively (Fig. S13). Zeeman splitting of the pseudospin doublets was described using the g_{zz} value of the **g** tensors obtained from the averaged crystal field calculations (Fig. S14). The magnetic field was oriented along the z-axis. The values of $\boldsymbol{J}_{rad-Ln}$ for **2** and **3** were obtained from the fitted value of **1**, which was further scaled for **2** and **3** using the following relations $(7/2)^2*(2/6)^2$ and $(7/2)^2*(2/5)^2$, respectively. We wish to note that the omission of the excited (pseudo) doublets of Ln^{III} ions from the simulation and the utilization of scaled exchange coupling parameters for **2** and **3** mean that the results of the simulations are more qualitive than quantitative, but they give rough magnitudes for the energies of the low-lying exchange doublets.

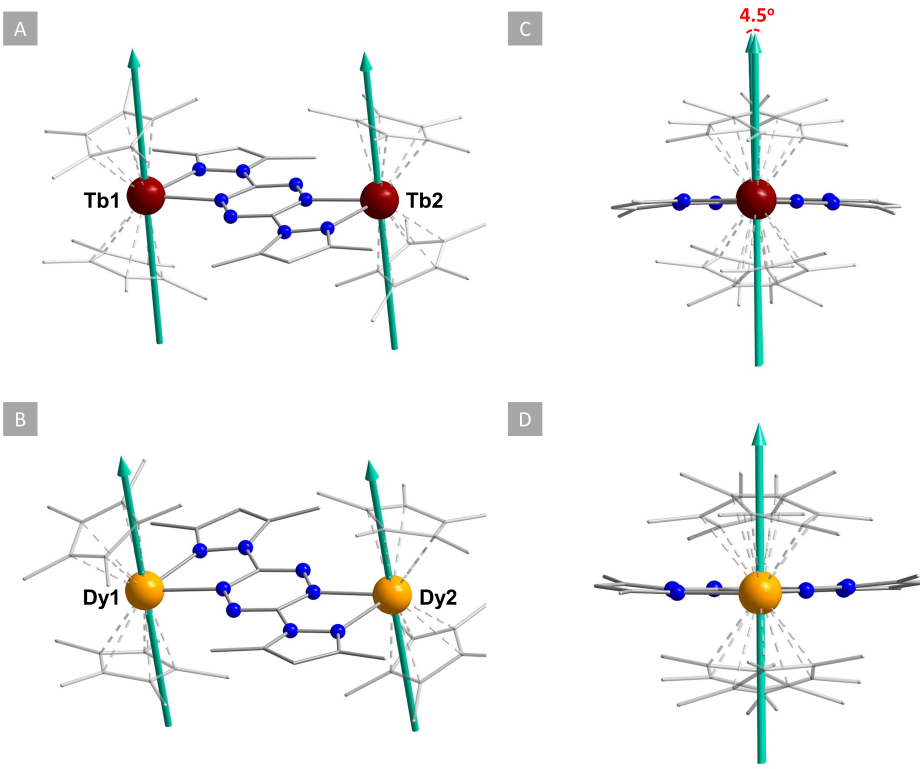

Fig. S13. Different views of the orientation of the *ab initio* calculated principal magnetic axes (teal vectors) of the ground Kramers doublet for **2** (top, A and C) and **3** (bottom, B and D).

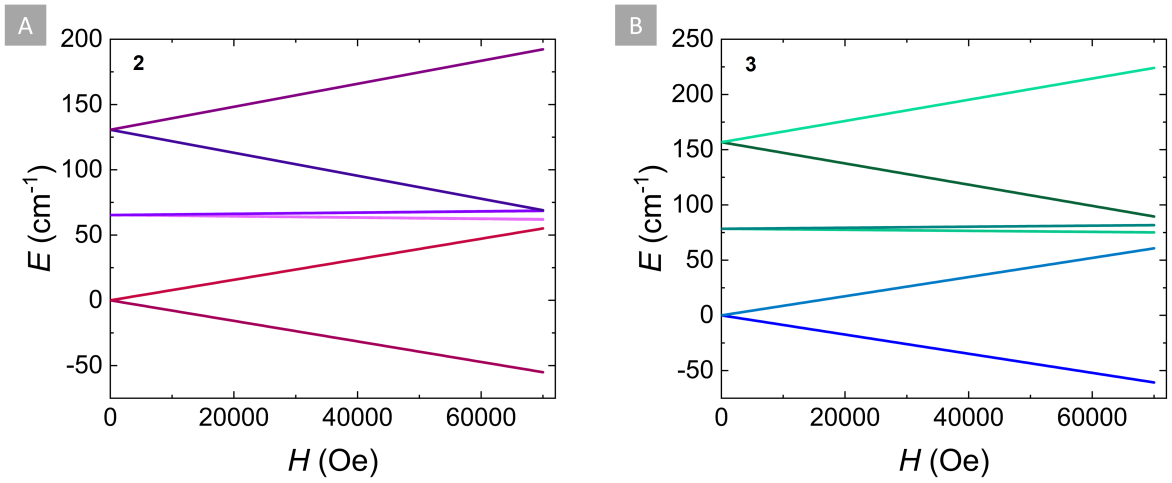

Fig. S14. The splitting of the low-lying exchange states of **2** (A) and **3** (B) under an external magnetic field applied along the principal magnetic axes shown for all states considered in the spin model (A for **2** and B for **3**) For both, **2** and **3**, the ground exchange doublet corresponds to two ferrimagnetic states in which the spins of Ln^{III} centers are oriented to the same direction and the spin of the radical ligand to the opposite direction. The second exchange doublet is a four-fold degenerate and the spin of the one Ln^{III} center is flipped with the respect the ground state spin orientation. The third exchange doublet is two-fold degenerate and correspond to the ferromagnetic state, that is, spins of the magnetic centers are oriented to the same direction.

The influence of configurational isomerism (*trans* vs. *cis*) and steric bulk of cyclopentadienyl ligands on the magnetic interactions of the reported complexes was investigated by carrying out the broken symmetry (BS) density functional theory (DFT) calculations for four different cationic gadolinium model systems – **1Cp*$_{trans}$**, **1Cp*$_{cis}$**, **1Cp$_{trans}$**, and **1Cp$_{cis}$** – that were constructed from the crystal structure of **1** (Cp* = pentamethylcylopentandienyl; Cp = cyclopentadienyl). The geometries of model systems were fully optimized without symmetry constraints in the gas-phase using the B3LYP[27] exchange-correlation functional in conjunction with the Cundari-Stevens[28] (CSDZ, for Gd) and def2-TZVPP[29] (for all other

atoms) basis sets. The dispersion force was modelled with the D3 empirical dispersion correction along with the damping function.[30] All geometries were converged to the intermediate spin state with S = 13/2 arising from the αβα (Gd^{III}-rad-Gd^{III}) spin configuration. The nature of the found minima on the potential energy hypersurface was confirmed by the frequency analyses (no negative frequencies). The optimized structures of **1Cp*$_{trans}$**, **1Cp*$_{cis}$** **1Cp$_{trans}$**, and **1Cp$_{cis}$** are given in Fig. 4 and S15, whereas their selected bond lengths and angles are given in Table S3.

Table S3. Selected bond lengths (Å) and angles (°) for the optimized structures of **1Cp*$_{trans}$**, **1Cp*$_{cis}$**, **1Cp$_{trans}$**, and **1Cp$_{cis}$**. Exp.–Opt. = the difference between the experimental and calculated data.

Bond/Angle	1Cp*$_{trans}$	Exp.–Opt.	1Cp$_{trans}$	Exp.–Opt.	1Cp*$_{cis}$	Exp.–Opt.	1Cp$_{cis}$	Exp.–Opt.
Gd1-Gd2$_{intra}$	7.591	-0.007	7.529	0.055	5.392	2.192	4.334	3.25
Gd1-N1$_{pyrazole}$	2.506	-0.079	2.489	-0.062	2.481	-0.054	2.461	-0.034
Gd1-N3$_{tetrazine}$	2.44	-0.031	2.416	-0.007	2.58	-0.171	2.478	-0.069
Gd2-N5$_{tetrazine}$	2.44	-0.005	2.416	0.019	2.759	-0.324	2.476	-0.041
Gd2-N8$_{pyrazole}$	2.506	-0.062	2.489	-0.045	2.503	-0.059	2.461	-0.017
Gd1- Cp$_{cent}$A	2.425	0.02	2.419	0.026	2.452	-0.007	2.457	-0.012
Gd1-Cp$_{cent}$B	2.427	0.006	2.408	0.025	2.442	-0.009	2.429	0.004
Gd2-Cp$_{cent}$C	2.425	0.01	2.419	0.016	2.503	-0.068	2.459	-0.024
Gd2-Cp$_{cent}$D	2.427	0.012	2.408	0.031	2.527	-0.088	2.429	0.01
Cp$_{cent}$A-Gd1-Cp$_{cent}$B	148.72	-6.74	134.04	7.94	148.74	-6.76	132.19	9.79
Cp$_{cent}$C-Gd2-Cp$_{cent}$D	148.72	-7.57	134.04	7.11	130.38	10.77	154.72	-13.57
N1-Gd1-N3	64.39	0.5	64.61	0.28	67.85	-2.96	65.33	-0.44
N5-Gd2-N8	64.39	0.63	64.61	0.41	64.37	0.65	65.29	-0.27
Gd1-N3-N4-Gd1	178.94	-0.1	177.51	1.33	80.81	98.03	32.86	145.98

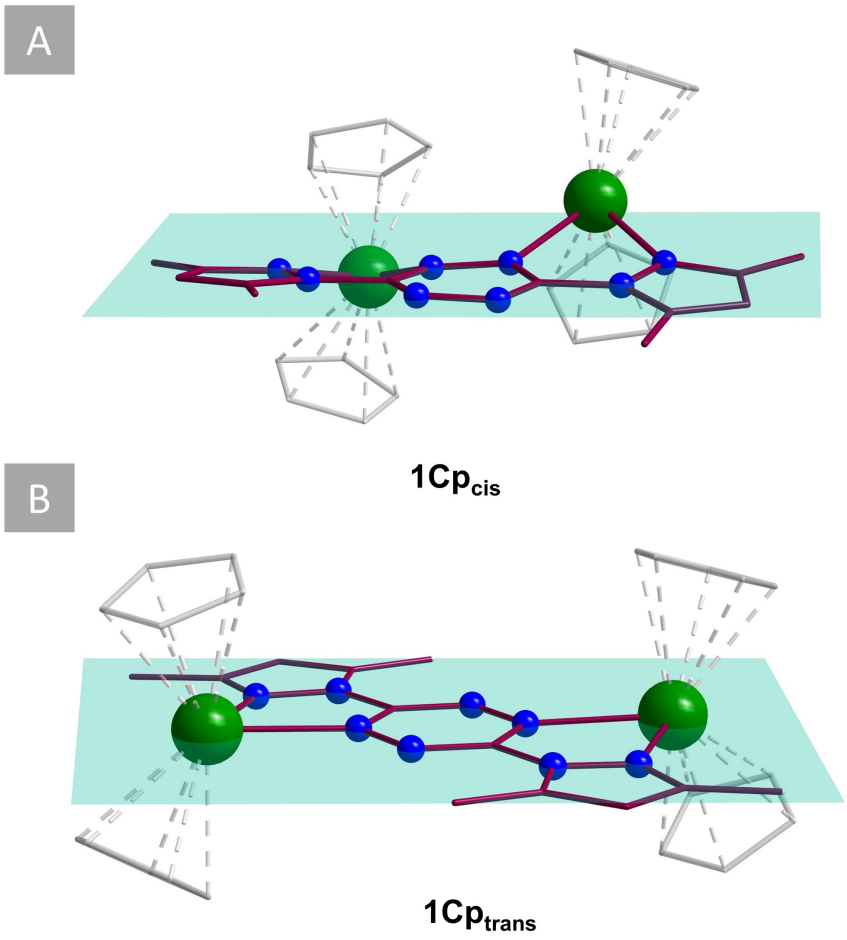

Fig. S15: Gas-phase optimized geometries of **1Cp$_{cis}$** (A) and **1Cp$_{trans}$** (B) as obtained from the B3LYP-D3/def2-TZVPP/CSDZ calculations, illustrating the strong twisting of the bpytz$^{\bullet-}$ in the *cis*-coordination mode *vs.* the *trans*-coordination mode where the ligand preserves its planarity. H-atoms were omitted for clarity.

To obtain the Gd^{III}–rad ($J_{Gd\text{-}rad}$) and Gd^{III}-Gd^{III} ($J_{Gd\text{-}Gd}$) exchange coupling constants for the optimized model systems, the scalar relativistic single point BS DFT calculations were performed using the CAM-B3LYP exchange correlation functional in conjunction with the SARC-ZORA-def2-TZVPP (for Gd) and ZORA-def2-TZVPP (for all other atoms) basis sets.[29a,31] The scalar relativistic effects were treated by the zeroth order regular approximation (ZORA).[32] Although the optimized geometry of **1Cp*$_{trans}$** was in a reasonable agreement with **1** (Table S3 and Fig. 4), the BS DFT calculations were also carried out for the crystal structure of **1** to ensure that small geometrical changes around the coordination environment of metal center during the optimization does not considerably affect the values of exchange coupling constants. Similar values obtained for **1Cp*$_{trans}$** and **1** confirmed that the calculated exchange coupling constants for the optimized geometries are valid (*vide infra*). Before the final BS DFT calculations, the positions of the hydrogen atoms in **1** were optimized at the DFT level, while the positions of all other atoms were frozen to their crystal-structure coordinates. Because the energies of the BS states can be interpreted as the expectation values of Ising states that diagonalize the Heisenberg–Dirac–van Vleck (HDvV),[33] the following Hamiltonian:

$$\hat{H}_{HDvV} = -2\boldsymbol{J}_{rad-Gd}\left(\hat{\boldsymbol{S}}_{rad}\cdot\hat{\boldsymbol{S}}_{Gd1} + \hat{\boldsymbol{S}}_{rad}\cdot\hat{\boldsymbol{S}}_{Gd2}\right) - 2\boldsymbol{J}_{Gd1-Gd2}\left(\hat{\boldsymbol{S}}_{Gd1}\cdot\hat{\boldsymbol{S}}_{Gd2}\right)$$

was used to evaluate the $J_{Gd\text{-}rad}$ and $J_{Gd\text{-}Gd}$ couplings in **1** and model systems. To simplify equations, it was further assumed that $J_{rad\text{-}Gd1} \approx J_{rad\text{-}Gd2}$ although the asymmetric unit of **1** contains two slightly different Gd^{III} centers and *cis* isomers belong to the point group with the lowest symmetry (C_1). For **1Cp*$_{trans}$** and **1Cp$_{trans}$** the above assumption is valid because they have a pseudo C_2 symmetry axis. To extract two different exchange coupling constants from the energy differences of BS states, the energies of three different spin states were calculated for each complex. The states were: $E_{\alpha\alpha\alpha} = E_{HS}$ (high spin state), $E_{\alpha\beta\alpha} = E_{IS}$ (intermediate spin state), and $E_{\alpha\alpha\beta} = E_{LS}$ (low spin state). The calculated energies of BS states are given in Table S4.

Table S4. Energies of the optimized model systems (B3LYP-D3/def2-TZVPP/CSDZ) as well as energies of three BS states (CAM-B3LYP/SARC-ZORA-def2-TZVPP). All energies are given in Hartrees.

			B3LYP-D3/def2-TZVPP/CSDZ		
State	**1Cp*$_{trans}$**	**1Cp$_{trans}$**	**1Cp*$_{cis}$**	**1Cp$_{cis}$**	**1**
E_{IS}	-3997.100040350	-3210.317146570	-3997.057647920	-3210.311638910	-3997.04914938
			CAM-B3LYP/SARC-ZORA-def2-TZVPP		
State	**1Cp*$_{trans}$**	**1Cp$_{trans}$**	**1Cp*$_{cis}$**	**1Cp$_{cis}$**	**1**
E_{HS}	-25512.311179890	-24725.696495778	-25512.247707535	-24725.669052508	-25512.256131589
E_{IS}	-25512.312583540	-24725.697752513	-25512.248020525	-24725.669735378	-25512.257681316
E_{LS}	-25512.311884487	-24725.697126690	-25512.247887394	-24725.669394951	-25512.256874277

From the calculated energies, the values of the exchange coupling constants $J_{Gd\text{-}rad}$ and $J_{Gd\text{-}Gd}$ were obtained as:

$$J_{rad-Gd} = \frac{E_{IS}-E_{HS}}{14},$$

$$J_{Gd-Gd} = \frac{2E_{LS}-E_{HS}-E_{IS}}{98}.$$

The calculated $J_{Gd\text{-}rad}$ exchange coupling constants for **1Cp*$_{trans}$** (-11.07 cm^{-1}) and **1** (-11.67 cm^{-1}) are in a reasonable agreement with the value (-14.0 cm^{-1}) obtained from the fit confirming the validity of the used computational method and the antiferromagnetic nature of the Gd^{III}–rad interaction (Table S5). For all investigated complexes the calculated values of $J_{Gd\text{-}Gd}$ are within the error limits of BS DFT method, and no reliable conclusions can be drawn from them.

Table S5. Calculated exchange coupling constants $J_{Gd\text{-}rad}$ and $J_{Gd\text{-}Gd}$ for the model complexes (**1Cp*$_{trans}$**–**1Cp$_{cis}$**) and crystal structure of **1**.

	1Cp*$_{trans}$ (cm^{-1})	**1Cp$_{trans}$ (cm^{-1})**	**1Cp*$_{cis}$ (cm^{-1})**	**1Cp$_{cis}$ (cm^{-1})**	**1 (cm^{-1})**
$J_{Gd\text{-}rad}$	-11.07	-9.91	-2.83	-5.65	-11.67
$J_{Gd\text{-}Gd}$	-0.01	-0.02	-0.10	-0.21	0.14

To get further insight for the different magnetic properties of **3** and previously reported **Dy$_4$**, we also optimized the geometries of tz$^{\bullet-}$ and bpytz$^{\bullet-}$ at the B3LYP-D3/def2-TZVPP level of theory, calculated NBO charges for **1Cp*$_{trans}$**, bpytz$^{\bullet-}$, and tz$^{\bullet-}$ as well as visualized their spin densities. The spin density distribution arising from the unpaired electron of the bridging bpytz$^{\bullet-}$ radical ligand in **1Cp*$_{trans}$** is mainly localized on the central tetrazine ring and only a minute amount of the spin density is found on the pyrazolyl rings (Fig. S16). The same can be concluded from the spin density distributions of tz$^{\bullet-}$ and bpytz$^{\bullet-}$ ligands, that is, in all compounds the unpaired electron of the bridging radical ligand is strongly localized on the central tetrazine ring. Because both bridging ligands tz$^{\bullet-}$ and bpytz$^{\bullet-}$ show equal spin density distribution, it is more likely that the effective charges of the coordination atoms and coordination mode play more important role in the different relaxation processes of **3** and **Dy$_4$** than the spin density distribution. Indeed, the calculated NBO charges show that the effective charges of coordination nitrogen atoms in pyrazolyl rings are lower if compared to the effective charges of nitrogen atoms of tetrazine rings (Table S6). The dissimilar charge distribution of tz$^{\bullet-}$ and bpytz$^{\bullet-}$ combined with their different coordination modes generate dissimilar crystal fields around Dy^{III} ions in **Dy$_4$** and **3**, respectively, resulting in the appearance of QTM process in **3** but not in **Dy$_4$**. Indeed, the calculated crystal field parameters for each metal site in **3** and **Dy$_4$** reveal that the B_{20} diagonal parameters of Dy^{III} ions in **3** (~350 cm^{-1}) are larger than in **Dy$_4$** (~230 cm^{-1}) which should enhance the axiality of **3** compared to **Dy$_4$.** However, off-diagonal parameters B_{22} of **3** (~260 cm^{-1}) are also larger than those obtained for **Dy$_4$** (~50–114 cm^{-1}) that significantly diminishes the axiality of **3**. The crystal field parameters with higher ranks are also dissimilar in **3** and **Dy$_4$**, but largest differences are observed in rank 2 parameters.

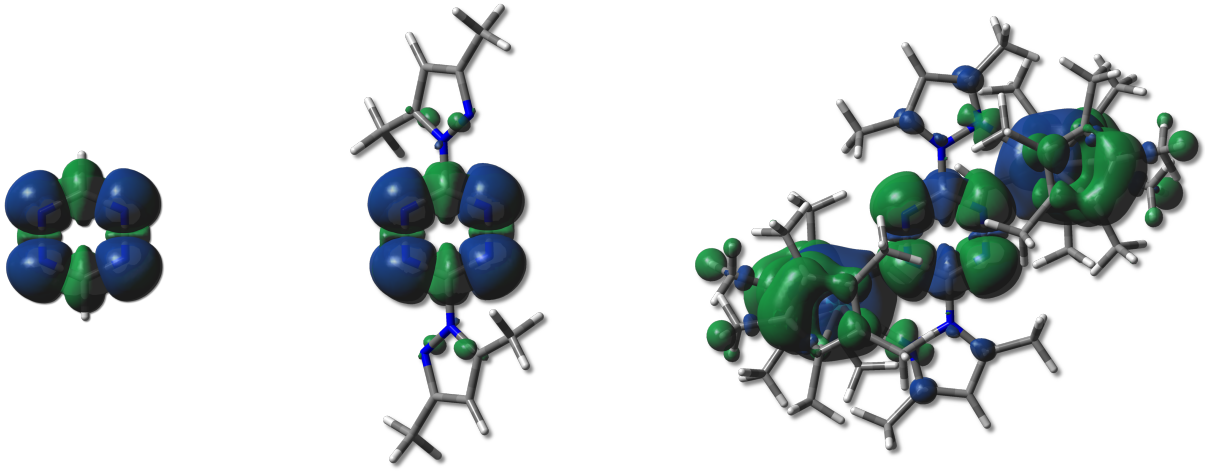

tz$^{\bullet-}$ **bpytz$^{\bullet-}$** **1Cp*$_{trans}$**

Fig. S16: Spin density distribution for the gas-phase optimized structures of tz$^{\bullet-}$, bpytz$^{\bullet-}$, and intermediate state (S=13/2) of **1Cp*$_{trans}$** calculated at the B3LYP/def2-TZVPP level of theory (blue = *α* spin density, green = *β* spin density, isovalue of the spin density surface = 0.0005). The *β* density on the Cp* ligands of **1Cp*$_{trans}$** originates from the spin polarization effect induced by *α* electrons of Gd^{III} ions.

Table S6. Calculated NBO charges for the selected atoms of tz$^{\bullet-}$, bpytz$^{\bullet-}$, and **1Cp*$_{trans}$** (*S* = 13/2).

atom	tz$^{\bullet-}$	bpytz$^{\bullet-}$	1Cp*$_{trans}$ (S=13/2)
$N1_{pyrazole}$	-	-0.255	-0.342
$N3_{tetrazine}$	-0.395	-0.337	-0.395
$N4_{tetrazine}$	-0.395	-0.369	-0.321
$N5_{tetrazine}$	-0.395	-0.337	-0.395
$N6_{tetrazine}$	-0.395	-0.369	-0.321
$N8_{pyrazole}$	-	-0.255	-0.342

Table S7. Energies of the thirteen lowest local spin-orbit (SO) states of the Tb1 ion in **2** arising from the crystal splitting of the $^6F_6$ ground multiplet as well as the angle between the magnetic axes of the ground and given excited doublet. For the pseudo doublets also the **g**-tensors and tunneling splitting are reported.

SO state	E / cm^{-1}	*Δ* / cm^{-1}	g_x	g_y	g_z	*θ*
1	0.000	0.240	0.000	0.000	17.826	-
2	0.240					
3	113.080	4.180	0.000	0.000	14.505	173.287
4	117.260					
5	228.960	23.480	0.000	0.000	10.974	2.911
6	252.440					
7	329.400	47.150	0.000	0.000	7.349	14.491
8	376.550					
9	404.090	-	-	-	-	-
10	530.810	3.610	0.000	0.000	14.597	88.223
11	534.420					
12	734.040	0.700	0.000	0.000	17.910	93.318
13	734.740					

Table S8. Energies of the thirteen lowest local spin-orbit (SO) states of the Tb2 ion in **2** arising from the crystal splitting of the $^6F_6$ ground multiplet as well as the angle between the magnetic axes of the ground and given excited doublet. For the pseudo doublets also the **g**-tensors and tunneling splitting are reported.

SO state	E / cm^{-1}	Δ / cm^{-1}	g_x	g_y	g_z	θ
1	0.000	0.130	0.000	0.000	17.876	-
2	0.130					
3	115.050	2.290	0.000	0.000	14.712	176.501
4	117.340					
5	248.340	15.120	0.000	0.000	11.415	3.667
6	263.460					
7	359.730	27.630	0.000	0.000	7.683	16.826
8	387.360					
9	423.880	-	-	-	-	-
10	522.210	5.240	0.000	0.000	14.306	89.715
11	527.450					
12	682.600	1.250	0.000	0.000	17.817	93.766
13	683.850					

Table S9. Energies and **g**-tensors of the eight lowest local KDs of the Dy1 ion in **3** arising from the crystal splitting of the $^6H_{15/2}$ ground multiplet as well as the angle between the magnetic axes of the ground and given excited doublet.

KD	E / cm^{-1}	g_x	g_y	g_z	θ
KD1	0.000	0.03	0.07	19.57	-
KD2	195.15	1.55	5.02	13.35	3.53
KD3	252.50	1.25	3.67	12.26	95.31
KD4	359.10	4.04	6.71	8.22	164.98
KD5	435.75	2.50	2.66	11.24	91.64
KD6	514.44	0.06	0.11	14.56	87.72
KD7	645.26	0.04	0.05	17.31	87.88
KD8	972.74	0.00	0.00	19.99	90.19

Table S10. Energies and **g**-tensors of the eight lowest local KDs of the Dy2 ion in **3** arising from the crystal splitting of the $^6H_{15/2}$ ground multiplet as well as the angle between the magnetic axes of the ground and given excited doublet.

KD	E / cm^{-1}	g_x	g_y	g_z	θ
KD1	0.00	0.02	0.05	19.59	-
KD2	190.36	1.30	3.82	14.21	2.66
KD3	245.74	0.34	3.43	13.49	94.58
KD4	340.12	4.08	6.83	8.00	7.73
KD5	413.11	2.47	2.56	11.26	89.01
KD6	491.28	0.10	0.13	14.58	90.74
KD7	617.96	0.03	0.03	17.30	90.90
KD8	918.64	0.00	0.00	19.98	89.88

Table S11. Calculated low-lying exchange energy levels given in cm^{-1} for **2** and **3** obtained by the Hamiltonian 1.

State	*2*	State	*3*
1	0	1	0
2	65.33	2	78.40
3	65.33	3	78.40
4	130.67	4	156.80

Table S12. Calculated *ab initio* crystal-field parameters (cm^{-1}) given in the Iwahara–Chibotaru notation[34] for Tb1 in **2**. "Neutral" and "double anion" refers to calculations where the $bpytz^{\bullet-}$ ligand was treated as a neutral and double anion, respectively, whereas "average" are the final crystal field parameters derived from the crystal field parameters of double anion and neutral.

		Neutral			***Double anion***			***Average***		
k	***q***	***Re(B_{kq})***	***Im(B_{kq})***	***$\|B_{kq}\|$***	***Re(B_{kq})***	***Im(B_{kq})***	***$\|B_{kq}\|$***	***Re(B_{kq})***	***Im(B_{kq})***	***$\|B_{kq}\|$***
2	0	-459.91	0.00	459.91	-245.81	0.00	245.81	-352.86	0.00	352.86
2	1	-2.10	3.70	4.26	23.68	-1.27	23.71	10.79	1.22	10.86
2	2	-207.46	-31.41	209.82	51.07	312.03	316.18	-78.19	140.31	160.63
4	0	52.58	0.00	52.58	-6.56	0.00	6.56	23.01	0.00	23.01
4	1	1.19	-1.21	1.69	-14.13	-15.95	21.31	-6.47	-8.58	10.75
4	2	8.58	-5.48	10.18	-5.34	6.41	8.35	1.62	0.47	1.69
4	3	-0.43	0.82	0.93	10.12	15.73	18.70	4.85	8.28	9.59
4	4	-4.43	-25.78	26.16	-15.04	8.08	17.07	-9.74	-8.85	13.16
6	0	2.19	0.00	2.19	5.02	0.00	5.02	3.61	0.00	3.61
6	1	0.03	-0.47	0.47	7.07	3.38	7.84	3.55	1.46	3.84
6	2	2.60	1.70	3.10	0.17	-4.20	4.20	1.38	-1.25	1.86
6	3	0.34	-0.23	0.41	1.67	-0.57	1.76	1.00	-0.40	1.08
6	4	-0.60	1.86	1.96	-2.16	-0.45	2.20	-1.38	0.71	1.55
6	5	0.30	-0.56	0.64	-0.49	-1.42	1.51	-0.10	-0.99	1.00
6	6	-0.27	7.66	7.67	1.11	4.74	4.86	0.42	6.20	6.21
8	0	-0.48	0.00	0.48	-0.64	0.00	0.64	-0.56	0.00	0.56
8	1	-0.01	0.10	0.10	-0.40	-0.57	0.70	-0.20	-0.24	0.31
8	2	-0.38	-0.21	0.43	0.12	0.34	0.37	-0.13	0.07	0.14
8	3	-0.03	0.00	0.03	-0.20	-0.22	0.30	-0.11	-0.11	0.16
8	4	0.04	-0.12	0.13	0.11	-0.02	0.12	0.08	-0.07	0.11
8	5	-0.03	0.03	0.04	-0.01	0.14	0.14	-0.02	0.08	0.09
8	6	0.03	-0.22	0.22	-0.05	-0.17	0.18	-0.01	-0.20	0.20
8	7	-0.01	0.01	0.02	0.08	-0.05	0.10	0.04	-0.02	0.04
8	8	0.03	-0.21	0.21	-0.31	0.12	0.33	-0.14	-0.04	0.14
10	0	0.02	0.00	0.02	0.02	0.00	0.02	0.02	0.00	0.02
10	1	0.00	-0.01	0.01	0.00	0.00	0.00	0.00	0.00	0.00
10	2	0.02	0.01	0.02	-0.01	-0.01	0.01	0.01	0.00	0.01
10	3	0.00	0.00	0.00	0.00	0.01	0.01	0.00	0.00	0.00
10	4	0.00	0.00	0.00	0.00	0.00	0.00	0.00	0.00	0.00
10	5	0.00	0.00	0.00	0.00	-0.01	0.01	0.00	0.00	0.01
10	6	0.00	0.01	0.01	0.00	0.00	0.00	0.00	0.00	0.00
10	7	0.00	0.00	0.00	0.00	0.00	0.00	0.00	0.00	0.00
10	8	0.00	0.00	0.00	0.01	0.00	0.01	0.00	0.00	0.00
10	9	0.00	0.00	0.00	0.00	0.00	0.00	0.00	0.00	0.00
10	10	0.00	0.00	0.00	0.00	-0.01	0.01	0.00	0.00	0.00

Table S13. Calculated *ab initio* crystal-field parameters (cm^{-1}) given in the Iwahara–Chibotaru notation[34] for Tb2 in **2**. "Neutral" and "double anion" refers to calculations where the $bpytz^{\bullet-}$ ligand was treated as a neutral and double anion, respectively, whereas "average" are the final crystal field parameters derived from the crystal field parameters of double anion and neutral.

		Neutral			*Double anion*			*Average*		
k	***q***	***Re(B_{kq})***	***Im(B_{kq})***	***$\|B_{kq}\|$***	***Re(B_{kq})***	***Im(B_{kq})***	***$\|B_{kq}\|$***	***Re(B_{kq})***	***Im(B_{kq})***	***$\|B_{kq}\|$***
2	0	-447.24	0.00	447.24	-262.43	0.00	262.43	-354.83	0.00	354.83
2	1	-1.95	-2.67	3.31	-14.39	-9.07	17.01	-8.17	-5.87	10.06
2	2	-144.42	-185.00	234.69	-68.89	310.30	317.85	-106.65	62.65	123.69
4	0	53.11	0.00	53.11	-8.48	0.00	8.48	22.32	0.00	22.32
4	1	1.37	1.48	2.02	10.18	16.55	19.43	5.77	9.01	10.70
4	2	11.58	2.85	11.93	-7.53	10.47	12.90	2.03	6.66	6.96
4	3	-2.20	-0.22	2.21	2.19	-11.00	11.21	-0.01	-5.61	5.61
4	4	27.24	-3.80	27.50	-18.70	-6.35	19.75	4.27	-5.08	6.63
6	0	2.55	0.00	2.55	8.77	0.00	8.77	5.66	0.00	5.66
6	1	0.12	-0.09	0.15	-5.77	-4.51	7.32	-2.82	-2.30	3.64
6	2	0.38	3.07	3.09	0.98	-3.60	3.73	0.68	-0.27	0.73
6	3	0.23	0.42	0.48	-1.04	-0.03	1.04	-0.40	0.20	0.45
6	4	-1.97	-0.85	2.15	-1.87	-1.66	2.50	-1.92	-1.25	2.29
6	5	0.15	-0.07	0.16	-0.08	0.61	0.62	0.03	0.27	0.27
6	6	-5.40	-6.28	8.28	-3.57	3.86	5.26	-4.49	-1.21	4.65
8	0	-0.54	0.00	0.54	-0.67	0.00	0.67	-0.60	0.00	0.60
8	1	-0.01	0.01	0.01	0.30	0.57	0.64	0.14	0.29	0.32
8	2	-0.05	-0.47	0.47	-0.04	0.41	0.41	-0.05	-0.03	0.06
8	3	-0.01	-0.03	0.04	-0.03	0.24	0.24	-0.02	0.10	0.11
8	4	0.13	0.06	0.14	0.10	0.04	0.11	0.12	0.05	0.12
8	5	0.00	0.00	0.00	0.07	-0.04	0.08	0.03	-0.02	0.04
8	6	0.12	0.21	0.24	0.16	-0.18	0.24	0.14	0.01	0.14
8	7	-0.01	0.00	0.01	-0.05	-0.01	0.06	-0.03	-0.01	0.03
8	8	-0.05	0.25	0.25	-0.20	-0.30	0.36	-0.12	-0.03	0.13
10	0	0.03	0.00	0.03	0.03	0.00	0.03	0.03	0.00	0.03
10	1	0.00	0.00	0.00	0.00	0.01	0.01	0.00	0.00	0.00
10	2	0.00	0.02	0.02	-0.01	-0.01	0.01	0.00	0.01	0.01
10	3	0.00	0.00	0.00	0.00	0.00	0.00	0.00	0.00	0.00
10	4	0.00	0.00	0.01	0.00	0.00	0.00	0.00	0.00	0.00
10	5	0.00	0.00	0.00	-0.01	0.00	0.01	0.00	0.00	0.00
10	6	0.00	-0.01	0.01	0.00	0.01	0.01	0.00	0.00	0.00
10	7	0.00	0.00	0.00	0.00	0.00	0.00	0.00	0.00	0.00
10	8	0.00	0.00	0.00	0.00	0.00	0.00	0.00	0.00	0.00
10	9	0.00	0.00	0.00	0.00	0.00	0.00	0.00	0.00	0.00
10	10	0.00	0.00	0.00	0.01	0.00	0.01	0.00	0.00	0.01

Table S14. Calculated *ab initio* crystal-field parameters (cm^{-1}) given in the Iwahara–Chibotaru notation[34] for Dy1 in **3**. "Neutral" and "double anion" refers to calculations where the $bpytz^{\bullet-}$ ligand was treated as a neutral and double anion, respectively, whereas "average" are the final crystal field parameters derived from the crystal field parameters of double anion and neutral.

		Neutral			***Double anion***			***Average***		
k	***q***	***Re(B_{kq})***	***Im(B_{kq})***	***$\|B_{kq}\|$***	***Re(B_{kq})***	***Im(B_{kq})***	***$\|B_{kq}\|$***	***Re(B_{kq})***	***Im(B_{kq})***	***$\|B_{kq}\|$***
2	0	-435.46	0.00	435.46	-252.31	0.00	252.31	-343.88	0.00	343.88
2	1	-6.96	0.02	6.96	-5.89	2.53	6.41	-6.43	1.27	6.55
2	2	226.06	42.42	230.01	297.09	-30.10	298.61	261.58	6.16	261.65
4	0	-41.45	0.00	41.45	-31.13	0.00	31.13	-36.29	0.00	36.29
4	1	0.05	0.40	0.41	-0.63	-3.42	3.48	-0.29	-1.51	1.54
4	2	-16.31	4.67	16.97	-5.68	-4.29	7.12	-11.00	0.19	11.00
4	3	-0.29	-0.48	0.56	-2.76	-0.19	2.76	-1.53	-0.33	1.56
4	4	23.81	-17.74	29.69	26.21	18.05	31.83	25.01	0.16	25.01
6	0	-21.23	0.00	21.23	-6.75	0.00	6.75	-13.99	0.00	13.99
6	1	2.01	-0.40	2.05	1.28	2.70	2.99	1.65	1.15	2.01
6	2	22.01	1.15	22.04	29.81	1.07	29.83	25.91	1.11	25.93
6	3	-0.76	0.34	0.84	-0.86	3.63	3.73	-0.81	1.98	2.14
6	4	4.13	3.51	5.42	0.60	0.73	0.94	2.36	2.12	3.17
6	5	1.71	0.58	1.81	-1.02	2.61	2.80	0.35	1.60	1.63
6	6	19.20	-11.82	22.55	15.32	12.94	20.05	17.26	0.56	17.27
8	0	0.99	0.00	0.99	1.05	0.00	1.05	1.02	0.00	1.02
8	1	-0.09	0.00	0.09	-0.03	0.10	0.11	-0.06	0.05	0.08
8	2	-0.69	0.01	0.69	-0.56	-0.04	0.56	-0.63	-0.02	0.63
8	3	-0.01	-0.01	0.01	-0.01	-0.14	0.14	-0.01	-0.07	0.07
8	4	-0.15	-0.12	0.19	-0.23	0.02	0.23	-0.19	-0.05	0.20
8	5	-0.01	-0.01	0.01	-0.01	0.00	0.01	-0.01	0.00	0.01
8	6	-0.04	0.05	0.06	-0.01	-0.01	0.02	-0.03	0.02	0.03
8	7	0.00	0.01	0.01	0.00	0.01	0.01	0.00	0.01	0.01
8	8	0.08	-0.02	0.08	0.08	0.04	0.09	0.08	0.01	0.08
10	0	-0.01	0.00	0.01	-0.01	0.00	0.01	-0.01	0.00	0.01
10	1	0.00	0.00	0.00	0.00	-0.01	0.01	0.00	-0.01	0.01
10	2	-0.02	-0.01	0.02	-0.03	0.00	0.03	-0.02	0.00	0.02
10	3	0.00	0.00	0.00	0.00	0.00	0.00	0.00	0.00	0.00
10	4	-0.01	0.00	0.01	-0.01	0.00	0.01	-0.01	0.00	0.01
10	5	0.00	0.00	0.00	0.00	0.00	0.00	0.00	0.00	0.00
10	6	-0.01	0.01	0.02	0.00	0.00	0.00	-0.01	0.00	0.01
10	7	0.00	0.00	0.00	0.00	0.00	0.01	0.00	0.00	0.00
10	8	0.01	-0.01	0.02	0.02	0.01	0.02	0.01	0.00	0.02
10	9	0.00	0.00	0.00	0.00	0.00	0.00	0.00	0.00	0.00
10	10	0.01	-0.02	0.02	0.00	0.02	0.02	0.01	0.00	0.01

Table S15. Calculated *ab initio* crystal-field parameters (cm^{-1}) given in the Iwahara–Chibotaru notation[34] for Dy2 in **3**. "Neutral" and "double anion" refers to calculations where the $bpytz^{\bullet-}$ ligand was treated as a neutral and double anion, respectively, whereas "average" are the final crystal field parameters derived from the crystal field parameters of double anion and neutral.

		Neutral			***Double anion***			***Average***		
k	***q***	***Re(B_{kq})***	***Im(B_{kq})***	***$\|B_{kq}\|$***	***Re(B_{kq})***	***Im(B_{kq})***	***$\|B_{kq}\|$***	***Re(B_{kq})***	***Im(B_{kq})***	***$\|B_{kq}\|$***
2	0	-421.73	0.00	421.73	-235.76	0.00	235.76	-328.74	0.00	328.74
2	1	1.29	-1.83	2.24	3.13	-1.30	3.39	2.21	-1.56	2.71
2	2	213.51	19.85	214.43	276.35	-32.67	278.28	244.93	-6.41	245.01
4	0	-39.63	0.00	39.63	-28.16	0.00	28.16	-33.90	0.00	33.90
4	1	0.84	0.70	1.09	-0.16	2.26	2.26	0.34	1.48	1.52
4	2	-13.31	11.68	17.71	-5.90	0.12	5.90	-9.60	5.90	11.27
4	3	1.84	0.08	1.84	1.28	0.97	1.61	1.56	0.52	1.65
4	4	18.19	-24.76	30.72	28.08	20.90	35.00	23.13	-1.93	23.21
6	0	-21.41	0.00	21.41	-6.77	0.00	6.77	-14.09	0.00	14.09
6	1	-0.67	0.08	0.68	-0.47	-1.86	1.92	-0.57	-0.89	1.06
6	2	19.74	-2.75	19.93	28.21	-0.52	28.22	23.97	-1.64	24.03
6	3	0.27	-0.86	0.91	0.61	-2.55	2.62	0.44	-1.71	1.76
6	4	5.10	1.12	5.23	1.15	0.15	1.16	3.13	0.64	3.19
6	5	-1.41	-0.41	1.46	0.78	-1.79	1.95	-0.31	-1.10	1.14
6	6	11.14	-20.68	23.48	16.36	13.13	20.98	13.75	-3.77	14.25
8	0	0.87	0.00	0.87	0.93	0.00	0.93	0.90	0.00	0.90
8	1	0.02	-0.01	0.03	0.00	-0.07	0.07	0.01	-0.04	0.04
8	2	-0.61	0.07	0.62	-0.50	-0.06	0.51	-0.56	0.00	0.56
8	3	0.00	0.02	0.02	0.00	0.09	0.09	0.00	0.06	0.06
8	4	-0.14	-0.05	0.15	-0.21	0.06	0.21	-0.17	0.00	0.17
8	5	0.01	0.00	0.01	0.00	-0.01	0.01	0.01	0.00	0.01
8	6	-0.03	0.05	0.06	-0.01	-0.02	0.02	-0.02	0.01	0.02
8	7	0.00	0.00	0.01	0.00	0.00	0.00	0.00	0.00	0.00
8	8	0.05	-0.06	0.08	0.08	0.04	0.09	0.06	-0.01	0.07
10	0	0.00	0.00	0.00	-0.01	0.00	0.01	-0.01	0.00	0.01
10	1	0.00	0.00	0.00	0.00	0.01	0.01	0.00	0.01	0.01
10	2	-0.01	-0.01	0.01	-0.02	0.01	0.02	-0.02	0.00	0.02
10	3	0.00	0.00	0.00	0.00	0.00	0.00	0.00	0.00	0.00
10	4	-0.01	0.01	0.02	-0.01	0.00	0.01	-0.01	0.00	0.01
10	5	0.00	0.00	0.00	0.00	0.00	0.00	0.00	0.00	0.00
10	6	-0.01	0.02	0.02	0.00	0.00	0.00	0.00	0.01	0.01
10	7	0.00	0.00	0.00	0.00	0.00	0.00	0.00	0.00	0.00
10	8	0.01	-0.01	0.02	0.02	0.01	0.02	0.01	0.00	0.01
10	9	0.00	0.00	0.00	0.00	0.00	0.00	0.00	0.00	0.00
10	10	-0.01	-0.02	0.02	0.01	0.02	0.02	0.00	0.00	0.00

The isotropic hyperfine coupling constants (IHCC) were calculated for the selected atoms of **4** at the CAM-B3LYP-D3/(SARC)-ZORA-def2-TZVPP level of theory (Table S16). Prior to this single point calculation, the geometry of **4** was optimized at the B3LYP-D3/def2-TZVPP level of theory. In the geometry optimization, the core electrons of yttrium atoms were described by the effective core potential.[35] The calculated values correlated well with the ones obtained from the simulation of the EPR spectrum showing two slightly different IHCCs for the coordinated and non-coordinated nitrogen atoms.

Table S16. Calculated isotropic hyperfine coupling constants for the selected nitrogen and yttrium atoms of **4**.

Nucleus	mT	MhZ
$^{14}N3_{tetrazine}$	0.545	15.273
$^{14}N4_{tetrazine}$	0.452	12.659
$^{14}N5_{tetrazine}$	0.545	15.273
$^{14}N6_{tetrazine}$	0.452	12.659
$^{89}Y1$	0.142	3.967
$^{89}Y2$	0.142	3.967

All density functional theory calculations were performed with Gaussian 16[36] and ORCA (5.0.3)[37] quantum chemistry program packages.

Optimized geometry of 1Cp*$_{trans}$

Gd	-3.79175	-0.16850	0.01851
N	-2.81284	2.13746	0.06496
C	-5.00693	-1.46503	1.95178
C	-3.62826	-1.53922	2.30762
C	-3.21660	-0.25368	2.72628
C	-4.33215	0.61948	2.64296
C	-5.43642	-0.11334	2.15015
C	-5.88866	-2.63886	1.66407
H	-5.39804	-3.38591	1.03883
H	-6.81218	-2.34562	1.17109
H	-6.16710	-3.14298	2.59439
C	-2.81257	-2.79419	2.34610
H	-2.95916	-3.33110	3.28744
H	-1.74902	-2.58137	2.25352
H	-3.08553	-3.48288	1.54489
C	-1.86384	0.12488	3.23999
H	-1.84130	0.14136	4.33293
H	-1.56641	1.12012	2.90444
H	-1.09909	-0.57637	2.91279
C	-4.34010	2.03614	3.12519
H	-4.32945	2.06995	4.21760
H	-5.23013	2.57147	2.80104
H	-3.46845	2.59501	2.78250
C	-6.84377	0.38205	2.00382
H	-7.37371	-0.12428	1.19700
H	-6.88160	1.45225	1.79904
H	-7.42203	0.21457	2.91648
C	-5.40403	-0.97010	-1.92423
C	-4.16674	-1.65790	-2.12966
C	-3.22245	-0.71214	-2.60390
C	-3.85781	0.55358	-2.67236
C	-5.20091	0.39838	-2.25108
C	-6.73262	-1.59551	-1.64038
H	-6.63641	-2.56982	-1.16755
H	-7.28954	-1.74307	-2.57058
H	-7.35639	-0.97177	-0.99929
C	-3.95053	-3.13575	-2.00712
H	-2.93899	-3.37177	-1.67715
H	-4.09856	-3.64084	-2.96568
H	-4.64154	-3.59089	-1.29808
C	-1.83194	-1.01516	-3.06663
H	-1.18208	-0.14442	-2.98642

H	-1.82509	-1.32528	-4.11501
H	-1.37537	-1.81658	-2.48766
C	-3.22251	1.81013	-3.18163
H	-3.73596	2.70043	-2.82310
H	-3.23768	1.84750	-4.27387
H	-2.17862	1.89145	-2.87599
C	-6.28688	1.43082	-2.29063
H	-6.90292	1.42820	-1.38869
H	-6.96412	1.25175	-3.12987
H	-5.88599	2.43435	-2.41475
C	-3.29972	3.36743	0.01324
C	-2.24946	4.29614	-0.12964
H	-2.33416	5.36576	-0.20472
N	0.63577	1.22455	0.01260
C	-0.66823	1.08973	-0.01070
C	0.66805	-1.08953	-0.01076
N	-1.35435	-0.05650	-0.00831
N	-0.63595	-1.22435	0.01256
N	1.35418	0.05670	-0.00832
N	-1.44900	2.25602	-0.03888
N	1.44878	-2.25584	-0.03886
N	2.81264	-2.13738	0.06504
C	-1.08088	3.57647	-0.16622
C	3.29943	-3.36739	0.01345
C	2.24911	-4.29603	-0.12945
C	1.08059	-3.57628	-0.16613
C	-4.76022	3.63544	0.08709
H	-4.98292	4.31908	0.90555
H	-5.11332	4.09888	-0.83386
H	-5.32525	2.72016	0.24546
C	0.30439	4.08063	-0.33849
H	0.93708	3.82140	0.50574
H	0.76829	3.65460	-1.22609
H	0.27050	5.16250	-0.44427
C	4.75990	-3.63551	0.08746
H	5.32498	-2.72026	0.24579
H	4.98247	-4.31910	0.90600
H	5.11304	-4.09906	-0.83342
C	-0.30471	-4.08036	-0.33841
H	-0.27090	-5.16223	-0.44410
H	-0.93742	-3.82100	0.50577
H	-0.76855	-3.65436	-1.22606
H	2.33373	-5.36566	-0.20446
Gd	3.79179	0.16849	0.01850
C	5.00707	1.46504	1.95172
C	3.62841	1.53934	2.30755
C	3.21665	0.25384	2.72625
C	4.33212	-0.61940	2.64296
C	5.43645	0.11332	2.15014
C	5.88890	2.63878	1.66397
H	5.39833	3.38586	1.03870
H	6.81239	2.34546	1.17100
H	6.16738	3.14291	2.59428
C	2.81282	2.79437	2.34599
H	2.95941	3.33129	3.28732
H	1.74925	2.58164	2.25339
H	3.08585	3.48303	1.54478
C	1.86385	-0.12458	3.23997
H	1.84129	-0.14098	4.33291
H	1.56635	-1.11983	2.90449
H	1.09916	0.57669	2.91271
C	4.33997	-2.03605	3.12523

H	4.32936	-2.06983	4.21765
H	5.22994	-2.57147	2.80106
H	3.46826	-2.59486	2.78258
C	6.84377	-0.38219	2.00384
H	7.37378	0.12412	1.19707
H	6.88151	-1.45239	1.79902
H	7.42201	-0.21480	2.91653
C	5.40419	0.96985	-1.92424
C	4.16696	1.65774	-2.12974
C	3.22260	0.71203	-2.60395
C	3.85786	-0.55374	-2.67233
C	5.20097	-0.39863	-2.25104
C	6.73282	1.59516	-1.64041
H	6.63669	2.56951	-1.16765
H	7.28978	1.74261	-2.57061
H	7.35653	0.97142	-0.99926
C	3.95090	3.13562	-2.00729
H	2.93931	3.37176	-1.67753
H	4.09919	3.64066	-2.96583
H	4.64180	3.59070	-1.29811
C	1.83213	1.01513	-3.06673
H	1.18218	0.14446	-2.98640
H	1.82531	1.32511	-4.11515
H	1.37563	1.81667	-2.48787
C	3.22247	-1.81026	-3.18156
H	3.73585	-2.70059	-2.82300
H	3.23764	-1.84767	-4.27379
H	2.17857	-1.89148	-2.87592
C	6.28685	-1.43115	-2.29053
H	6.90289	-1.42853	-1.38858
H	6.96411	-1.25219	-3.12978
H	5.88589	-2.43466	-2.41459

Optimized geometry of 1Cp*$_{cis}$

Gd	2.62589	-0.33559	0.20685
N	2.95773	1.69632	-1.25328
C	4.27884	-2.73996	-0.28087
C	2.90685	-3.06423	-0.30133
C	2.31492	-2.38032	-1.40344
C	3.34682	-1.62614	-2.05387
C	4.55680	-1.86796	-1.36109
C	5.32469	-3.43545	0.52985
H	4.92379	-3.85994	1.44660
H	6.15246	-2.77917	0.79599
H	5.75434	-4.26129	-0.04608
C	2.28357	-4.13252	0.54663
H	2.77215	-5.09281	0.36682
H	1.22713	-4.26503	0.33056
H	2.37329	-3.93146	1.61597
C	0.95793	-2.61961	-1.99129
H	0.68465	-3.67121	-1.91420
H	0.95398	-2.36213	-3.04753
H	0.14780	-2.04441	-1.53287
C	3.17970	-0.91976	-3.36449
H	3.05910	-1.63836	-4.18043
H	4.04462	-0.30734	-3.60456
H	2.30645	-0.26721	-3.38195
C	5.94876	-1.57243	-1.83185
H	6.55835	-1.05088	-1.09228
H	5.95735	-0.98520	-2.74559

H	6.46550	-2.51003	-2.05087
C	3.85258	-0.42645	2.58760
C	2.59413	0.09600	2.98395
C	2.49744	1.41987	2.49956
C	3.69731	1.73498	1.81137
C	4.53691	0.59655	1.84253
C	4.47885	-1.64092	3.19069
H	3.82791	-2.51467	3.15390
H	4.69796	-1.45666	4.24718
H	5.41469	-1.90023	2.70827
C	1.71588	-0.53208	4.01978
H	0.69734	-0.15578	3.98684
H	2.10506	-0.31189	5.01852
H	1.67510	-1.61646	3.93114
C	1.39037	2.37674	2.81131
H	1.34575	3.19807	2.09989
H	1.52750	2.81924	3.80219
H	0.41788	1.88494	2.81832
C	4.05638	3.09229	1.29259
H	4.86530	3.05101	0.56728
H	4.39103	3.73709	2.10939
H	3.21320	3.59362	0.81818
C	5.98481	0.54047	1.46386
H	6.26426	-0.42159	1.03695
H	6.61767	0.69487	2.34236
H	6.24830	1.31302	0.74542
C	3.93720	2.20894	-1.99229
C	3.48028	3.34133	-2.69000
H	4.04186	3.94279	-3.38261
N	0.36388	1.16631	-0.27992
C	0.74179	2.40535	-0.63075
C	-1.43130	2.29247	0.65670
N	0.19209	3.54825	-0.29900
N	-0.94693	3.49162	0.44325
N	-0.89819	1.11126	0.31784
N	1.88015	2.52317	-1.44459
N	-2.68714	2.26964	1.30152
N	-3.65346	1.39265	0.88025
C	2.17274	3.53674	-2.32132
C	-4.77671	1.76115	1.48801
C	-4.52838	2.86702	2.32292
C	-3.19707	3.18463	2.18263
C	5.31497	1.66275	-1.98959
H	5.62228	1.36489	-2.99128
H	6.01562	2.42758	-1.65257
H	5.39766	0.80746	-1.33246
C	1.21950	4.58115	-2.77855
H	0.24728	4.15710	-3.02437
H	1.05475	5.32867	-2.00563
H	1.62586	5.06292	-3.66532
C	-6.07821	1.08629	1.23400
H	-5.94432	0.15797	0.68448
H	-6.58968	0.86541	2.16811
H	-6.72694	1.73651	0.64786
C	-2.40729	4.25313	2.84736
H	-2.97162	4.63588	3.69486
H	-1.44917	3.87662	3.20251
H	-2.19427	5.06824	2.15876
H	-5.23663	3.37101	2.95642
Gd	-2.73658	-0.59502	-0.28811
C	-2.29792	-2.96023	0.75157
C	-1.53457	-2.05762	1.55004

C	-2.42832	-1.34114	2.37788
C	-3.74176	-1.80118	2.11228
C	-3.67601	-2.77499	1.09416
C	-1.77771	-4.10032	-0.06399
H	-0.78222	-3.91010	-0.44941
H	-2.41988	-4.33224	-0.91170
H	-1.71852	-5.00592	0.54730
C	-0.04691	-1.91095	1.54803
H	0.43051	-2.56736	2.27590
H	0.23685	-0.88960	1.80544
H	0.37264	-2.16840	0.57654
C	-2.06077	-0.30454	3.39175
H	-1.76451	-0.75757	4.34117
H	-2.89440	0.36427	3.60023
H	-1.22818	0.30972	3.05259
C	-4.95470	-1.46576	2.91895
H	-5.01369	-2.11685	3.79541
H	-5.87652	-1.60751	2.35833
H	-4.93449	-0.44219	3.28838
C	-4.80706	-3.63499	0.62367
H	-4.62654	-4.03770	-0.37161
H	-5.75084	-3.09134	0.59189
H	-4.95251	-4.48902	1.29141
C	-2.98871	-1.20745	-2.82001
C	-2.18726	-0.02507	-2.87151
C	-3.00825	1.06877	-2.52454
C	-4.32045	0.58901	-2.28883
C	-4.31820	-0.81329	-2.45027
C	-2.59715	-2.56382	-3.31860
H	-1.55691	-2.80386	-3.10888
H	-2.72972	-2.62714	-4.40300
H	-3.21147	-3.34906	-2.88121
C	-0.77373	0.07680	-3.36497
H	-0.04160	0.20935	-2.56585
H	-0.66740	0.93058	-4.03546
H	-0.49049	-0.81049	-3.92611
C	-2.60047	2.50814	-2.51447
H	-3.04567	3.05856	-1.68537
H	-2.91365	3.01395	-3.43216
H	-1.52069	2.61958	-2.43792
C	-5.51272	1.46265	-2.06519
H	-6.36907	0.90068	-1.69897
H	-5.81898	1.93519	-3.00224
H	-5.30448	2.26670	-1.35915
C	-5.52149	-1.70639	-2.43858
H	-5.26494	-2.73581	-2.19596
H	-6.00925	-1.72066	-3.41704
H	-6.26967	-1.37838	-1.71647

Optimized geometry of 1Cp$_{trans}$

Gd	3.74478	0.38688	-0.01965
N	2.92599	-1.96105	-0.13718
C	4.46506	1.85240	2.04329
C	3.20809	1.35978	2.46121
C	3.33414	-0.02480	2.69364
C	4.67087	-0.39522	2.43316
C	5.37695	0.75761	2.02976
C	5.60379	1.77998	-1.44629
C	4.33432	2.19182	-1.90530
C	3.73218	1.09536	-2.57246

C	4.63630	0.00577	-2.51853
C	5.78949	0.43134	-1.82036
C	3.49075	-3.15904	-0.15836
C	2.49679	-4.15914	-0.14340
H	2.64816	-5.22391	-0.15690
N	-0.57120	-1.25785	-0.09201
C	0.72374	-1.05749	-0.09546
C	-0.72376	1.05748	-0.09544
N	1.34349	0.12892	-0.08237
N	0.57118	1.25783	-0.09194
N	-1.34351	-0.12893	-0.08241
N	1.56959	-2.17194	-0.10630
N	-1.56961	2.17192	-0.10618
N	-2.92601	1.96102	-0.13693
C	1.28209	-3.51844	-0.11109
C	-3.49078	3.15901	-0.15802
C	-2.49683	4.15912	-0.14316
C	-1.28212	3.51843	-0.11097
C	4.96978	-3.31606	-0.17679
H	5.32771	-3.69868	0.78006
H	5.27222	-4.02453	-0.94717
H	5.46685	-2.36729	-0.37236
C	-0.08075	-4.10891	-0.09064
H	-0.63695	-3.79536	0.79116
H	-0.66111	-3.79813	-0.95785
H	0.00847	-5.19258	-0.09008
C	-4.96981	3.31603	-0.17630
H	-5.46691	2.36725	-0.37174
H	-5.32763	3.69872	0.78057
H	-5.27235	4.02445	-0.94670
C	0.08072	4.10891	-0.09065
H	0.63699	3.79540	0.79112
H	0.66102	3.79810	-0.95789
H	-0.00851	5.19258	-0.09011
H	-2.64820	5.22389	-0.15663
Gd	-3.74476	-0.38691	-0.01968
C	-4.46468	-1.85272	2.04319
C	-3.20782	-1.35984	2.46114
C	-3.33418	0.02470	2.69364
C	-4.67100	0.39484	2.43318
C	-5.37681	-0.75814	2.02973
C	-5.60291	-1.78086	-1.44649
C	-4.33322	-2.19102	-1.90638
C	-3.73255	-1.09346	-2.57305
C	-4.63779	-0.00487	-2.51793
C	-5.79020	-0.43215	-1.81954
H	4.48177	-0.96494	-2.96156
H	6.67367	-0.15840	-1.63603
H	6.31273	2.39206	-0.91339
H	3.91204	3.17892	-1.80032
H	2.77372	1.10065	-3.06647
H	5.08685	-1.38400	2.54280
H	6.42807	0.81525	1.79816
H	4.71072	2.88029	1.83001
H	2.30957	1.94329	2.58268
H	2.54855	-0.68549	3.02292
H	-2.77431	-1.09739	-3.06751
H	-3.90984	-3.17775	-1.80231
H	-6.31096	-2.39406	-0.91370
H	-6.67491	0.15653	-1.63437
H	-4.48449	0.96630	-2.96038
H	-2.54873	0.68555	3.02294

H	-5.08720	1.38351	2.54287
H	-6.42792	-0.81601	1.79812
H	-4.71010	-2.88066	1.82988
H	-2.30917	-1.94316	2.58257

Optimized geometry of 1Cp$_{cis}$

Gd	-2.14598	-0.78383	0.31923
N	-3.30549	1.20300	-0.55655
C	-3.06500	-2.49562	2.29198
C	-2.27024	-1.51473	2.91679
C	-2.92769	-0.26579	2.78476
C	-4.14228	-0.49243	2.08362
C	-4.22109	-1.86539	1.78142
C	-1.97807	-3.07068	-1.00503
C	-0.81360	-2.42112	-1.47083
C	-1.20760	-1.34598	-2.29809
C	-2.61424	-1.33223	-2.35378
C	-3.09826	-2.39210	-1.55947
C	-4.55094	1.49370	-0.91176
C	-4.67431	2.87901	-1.12739
H	-5.55994	3.41052	-1.42737
N	-0.68331	1.17471	-0.08470
C	-1.25085	2.38295	-0.24341
C	1.25161	2.38448	0.25335
N	-0.66392	3.54976	-0.14556
N	0.65902	3.55026	0.17759
N	0.68714	1.17643	0.08669
N	-2.61949	2.39008	-0.54097
N	2.62456	2.39381	0.53090
N	3.31632	1.21001	0.51979
C	-3.44284	3.43955	-0.88836
C	4.57087	1.50547	0.83851
C	4.69277	2.88924	1.06209
C	3.45191	3.44501	0.86220
C	-5.59887	0.44776	-1.05325
H	-6.48590	0.71343	-0.47842
H	-5.90352	0.35477	-2.09669
H	-5.24532	-0.52109	-0.71306
C	-3.04853	4.86774	-0.98632
H	-2.69440	5.24943	-0.03085
H	-2.23673	5.01038	-1.69718
H	-3.91368	5.44320	-1.30784
C	5.63420	0.46816	0.91053
H	5.21375	-0.53336	0.91746
H	6.30744	0.54889	0.05564
H	6.23312	0.60007	1.81085
C	3.05298	4.87001	0.98462
H	3.92280	5.44656	1.29128
H	2.67433	5.25978	0.04188
H	2.25762	5.00102	1.71595
H	5.58321	3.42281	1.34351
Gd	2.14237	-0.78749	-0.31001
C	3.24946	-2.56144	-2.14314
C	2.28434	-1.79773	-2.82474
C	2.72932	-0.45148	-2.85596
C	3.98764	-0.40023	-2.19710
C	4.29931	-1.70093	-1.75408
C	1.88316	-3.04419	1.05526
C	0.78484	-2.31419	1.56252
C	1.28383	-1.25740	2.35491

C	2.68907	-1.33373	2.34763
C	3.06811	-2.43363	1.54921
H	-5.03336	-2.35630	1.27049
H	-2.01275	-3.96462	-0.40507
H	-2.84408	-3.54919	2.24053
H	0.19157	-2.76723	-1.29761
H	-1.34600	-1.68920	3.44192
H	-0.55174	-0.66673	-2.81776a
H	-2.60180	0.67384	3.20260
H	-3.21413	-0.63357	-2.91176
H	-4.12850	-2.68560	-1.44217
H	-4.88450	0.25500	1.86001
H	3.35684	-0.66816	2.86781
H	0.69706	-0.52619	2.88613
H	-0.24684	-2.60544	1.45268
H	1.83344	-3.94733	0.47005
H	4.07103	-2.79381	1.38788
H	3.20582	-3.62363	-1.96687
H	5.19725	-1.99547	-1.23607
H	4.60243	0.47740	-2.08737
H	2.24353	0.37007	-3.35890
H	1.38489	-2.17457	-3.28191

Optimized geometry of 4

C	4.73388	3.66477	0.05398
H	5.30970	2.75516	0.20293
H	4.95221	4.34569	0.87584
H	5.07809	4.13880	-0.86511
C	3.27568	3.38486	-0.01840
C	2.22301	4.30788	-0.17116
H	2.30461	5.37714	-0.25372
C	1.05706	3.58390	-0.20933
C	-0.32822	4.08111	-0.39715
H	-0.96908	3.81985	0.43995
H	-0.77935	3.65215	-1.28999
H	-0.29873	5.16289	-0.50434
C	0.65574	1.09531	-0.04072
C	-0.65574	-1.09531	-0.04069
C	0.32822	-4.08111	-0.39705
H	0.29872	-5.16290	-0.50423
H	0.96907	-3.81986	0.44007
H	0.77937	-3.65216	-1.28988
C	-1.05706	-3.58390	-0.20924
C	-2.22302	-4.30788	-0.17108
H	-2.30461	-5.37714	-0.25363
C	-3.27569	-3.38485	-0.01837
C	-4.73389	-3.66475	0.05393
H	-5.30972	-2.75515	0.20284
H	-4.95227	-4.34567	0.87579
H	-5.07805	-4.13879	-0.86518
C	4.22626	-1.68516	-2.01749
C	3.30177	-0.71978	-2.50390
C	3.95984	0.53677	-2.55157
C	5.29119	0.35105	-2.09332
C	5.46122	-1.02569	-1.78173
C	3.96813	-3.15797	-1.90586
H	2.98505	-3.36967	-1.48467
H	4.70644	-3.64975	-1.27497
H	4.00626	-3.64342	-2.88464

C	1.93123	-1.00745	-3.03387
H	1.97579	-1.31195	-4.08300
H	1.28362	-0.13256	-2.98117
H	1.44202	-1.80915	-2.48316
C	3.37690	1.79422	-3.11946
H	3.89772	2.68207	-2.76647
H	2.32326	1.91058	-2.86334
H	3.44139	1.79636	-4.21053
C	6.40479	1.35531	-2.12406
H	7.09060	1.14571	-2.94912
H	7.00443	1.34650	-1.21169
H	6.03440	2.36768	-2.26848
C	6.78374	-1.67113	-1.50959
H	7.35033	-1.76880	-2.43995
H	6.67848	-2.66867	-1.09233
H	7.40007	-1.08633	-0.82753
C	3.63617	-1.55967	2.22234
C	3.22565	-0.26145	2.62166
C	4.34977	0.60006	2.53068
C	5.45402	-0.16066	2.06136
C	5.01386	-1.50334	1.88465
C	2.81138	-2.80843	2.28349
H	1.74947	-2.59178	2.18170
H	2.95102	-3.32390	3.23776
H	3.08586	-3.51568	1.49964
C	1.88391	0.12181	3.16237
H	1.59244	1.12750	2.85474
H	1.88064	0.11328	4.25565
H	1.10609	-0.56400	2.83318
C	4.39008	2.00863	3.03770
H	3.51118	2.58253	2.74310
H	4.42527	2.01890	4.13021
H	5.27199	2.54180	2.68899
C	6.86662	0.32823	1.94093
H	7.39161	0.25976	2.89733
H	6.91686	1.37242	1.62927
H	7.43864	-0.25457	1.22112
C	5.87933	-2.69972	1.63496
H	6.07517	-3.22604	2.57312
H	6.84263	-2.42631	1.21408
H	5.41381	-3.41957	0.96134
C	-3.30179	0.71971	-2.50392
C	-3.95987	-0.53683	-2.55153
C	-5.29122	-0.35109	-2.09328
C	-5.46123	1.02566	-1.78174
C	-4.22627	1.68511	-2.01753
C	-1.93126	1.00735	-3.03391
H	-1.28365	0.13246	-2.98117
H	-1.44204	1.80907	-2.48325
H	-1.97583	1.31179	-4.08306
C	-3.37695	-1.79431	-3.11939
H	-3.44143	-1.79648	-4.21046
H	-3.89779	-2.68215	-2.76639
H	-2.32332	-1.91069	-2.86326
C	-6.40482	-1.35535	-2.12397
H	-7.00446	-1.34650	-1.21159
H	-6.03444	-2.36773	-2.26835
H	-7.09064	-1.14578	-2.94904
C	-6.78374	1.67113	-1.50961
H	-7.35032	1.76880	-2.43998
H	-6.67847	2.66867	-1.09236
H	-7.40009	1.08635	-0.82755

C	-3.96813	3.15793	-1.90595
H	-4.00631	3.64335	-2.88474
H	-2.98502	3.36963	-1.48480
H	-4.70640	3.64972	-1.27503
C	-3.22561	0.26151	2.62166
C	-4.34973	-0.60001	2.53072
C	-5.45400	0.16069	2.06139
C	-5.01385	1.50337	1.88464
C	-3.63616	1.55972	2.22232
C	-1.88387	-0.12172	3.16236
H	-1.10606	0.56410	2.83315
H	-1.59239	-1.12741	2.85474
H	-1.88058	-0.11318	4.25565
C	-4.39002	-2.00856	3.03779
H	-3.51112	-2.58246	2.74320
H	-5.27193	-2.54175	2.68912
H	-4.42518	-2.01879	4.13030
C	-6.86660	-0.32821	1.94097
H	-6.91682	-1.37246	1.62951
H	-7.43857	0.25447	1.22103
H	-7.39163	-0.25955	2.89734
C	-5.87934	2.69973	1.63493
H	-6.07517	3.22608	2.57307
H	-6.84264	2.42629	1.21407
H	-5.41384	3.41956	0.96128
C	-2.81137	2.80848	2.28341
H	-3.08589	3.51572	1.49957
H	-1.74946	2.59184	2.18158
H	-2.95098	3.32397	3.23768
N	2.79336	2.15181	0.03902
N	1.42850	2.26645	-0.07155
N	1.35605	-0.04201	-0.03401
N	0.64930	-1.21873	-0.01660
N	-0.64930	1.21873	-0.01664
N	-1.35605	0.04201	-0.03402
N	-1.42850	-2.26645	-0.07150
N	-2.79336	-2.15180	0.03906
Y	3.75062	-0.10080	0.02912
Y	-3.75062	0.10081	0.02913

Optimized geometry of $tz^{\bullet-}$

N	-0.70216	-1.20362	0.00003
N	0.69961	-1.20491	0.00002
C	1.25620	-0.00130	-0.00007
N	0.70243	1.20365	-0.00001
N	-0.69990	1.20506	0.00006
C	-1.25619	0.00123	-0.00006
H	2.34807	-0.00264	0.00019
H	-2.34805	0.00179	-0.00002

Optimized geometry of $bpytz^{\bullet-}$

N	3.43432	-1.01390	-0.07698
C	4.69017	-0.59329	-0.05221
C	4.74743	0.81452	0.06085
C	3.43377	1.23609	0.09661
N	2.67762	0.10698	0.01414
C	2.87157	2.60838	0.23229
C	5.81636	-1.56998	-0.14378

C	1.24809	0.03270	0.00700
N	0.67022	0.87805	-0.83081
N	-0.72019	0.84141	-0.84144
C	-1.24809	-0.03270	-0.00695
N	-0.67023	-0.87805	0.83086
N	0.72019	-0.84140	0.84148
N	-2.67762	-0.10698	-0.01410
C	-3.43377	-1.23608	-0.09679
C	-4.74743	-0.81452	-0.06101
C	-4.69017	0.59327	0.05230
N	-3.43433	1.01388	0.07717
C	-5.81638	1.56993	0.14411
C	-2.87152	-2.60832	-0.23271
H	-6.43948	1.38385	1.02270
H	-6.46625	1.51599	-0.73312
H	-5.41755	2.58083	0.21341
H	-5.62116	-1.44228	-0.11795
H	-2.14830	-2.66024	-1.04775
H	-3.67927	-3.31125	-0.43784
H	-2.34328	-2.90768	0.67079
H	2.14818	2.66041	1.04717
H	2.34352	2.90768	-0.67134
H	3.67932	3.31128	0.43751
H	5.62117	1.44229	0.11764
H	5.41749	-2.58079	-0.21428
H	6.46540	-1.51686	0.73411
H	6.44030	-1.38322	-1.02162

7. Additional ac magnetic data for complexes 1-3:

The ac behavior of **1** was explored by frequency-dependent measurements at 2 K with varying fields, in the frequency range of 0.1 to 1488 Hz. Between 0 and 400 Oe, no peak of the out-of-phase (χ'') susceptibility was observed. However, above 600 Oe, a signal was observed in the low-frequency (LF) region, which displayed field-dependance with the increase of the applied field. To accurately fit the data, the sum of two generalized Debye terms was employed to account for the presence of a second process in the high-frequency (HF) region (Fig. S17). However, despite our best efforts, since no peak of the susceptibility is observed (only tails) in the HF region, no reliable fitting parameters could be extracted for this process.

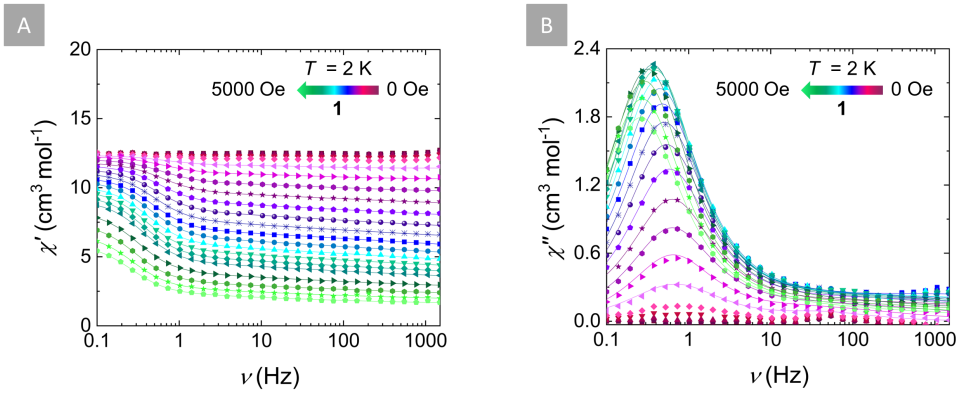

Fig. S17. The in-phase (χ') and out-of-phase (χ'') magnetic susceptibilities of **1** at 2 K in the field range of 0 to 5000 Oe. The solid lines represent best fits to the generalized Debye model.

Table S17. Best-fit parameters to the generalized Debye model obtained for the LF process for the frequency-dependence of the out-of-phase-magnetic susceptibility (χ'') as a function of the field for **1** collected at T = 2 K (Fig. S17).

H (Oe)	τ (s)	α	χ_s (cm^3 mol^{-1})	χ_t (cm^3 mol^{-1})
600	2.01 x 10^{-1}	1.14 x 10^{-2}	6.74	7.49
800	2.32 x 10^{-1}	1.32 x 10^{-2}	6.59	7.64
1000	2.42 x 10^{-1}	8.21 x 10^{-3}	6.37	7.86
1200	2.58 x 10^{-1}	1.41 x 10^{-2}	6.16	8.06
1400	2.73 x 10^{-1}	1.03 x 10^{-2}	5.89	8.34
1600	2.93 x 10^{-1}	1.03 x 10^{-2}	5.70	8.53
1800	3.18 x 10^{-1}	7.57 x 10^{-3}	5.49	8.74
2000	3.41 x 10^{-1}	1.26 x 10^{-2}	5.32	8.88
2200	3.60 x 10^{-1}	1.30 x 10^{-2}	5.21	9.02
2400	3.82 x 10^{-1}	1.15 x 10^{-2}	5.13	9.09
2600	4.08 x 10^{-1}	9.47 x 10^{-3}	5.03	9.20
2800	4.31 x 10^{-1}	1.02 x 10^{-2}	5.01	9.22
3000	4.55 x 10^{-1}	9.81 x 10^{-3}	4.98	9.25
3500	5.07 x 10^{-1}	1.49 x 10^{-2}	5.00	9.22
4000	5.56 x 10^{-1}	1.27 x 10^{-2}	5.01	9.13
4500	5.93 x 10^{-1}	2.94 x 10^{-2}	5.19	9.04
5000	6.19 x 10^{-1}	2.85 x 10^{-2}	5.33	8.80

Consequently, the extracted relaxation times of the magnetization (τ) for the LF process between 600 and 5000 Oe were obtained (Fig. S17, Table S17). As seen in Fig. S18, between 600 and 5000 Oe, the τ display an increase upon the increase of the applied dc field, without however reaching a maximum. This indicates that, as expected, the application of the constantly increasing field is contributing to the suppression of QTM, without however eliminating it even in the presence of an applied static field of 5000 Oe. Consequently, no optimal field could be selected. Indeed, a reliable fit of the field-dependent relaxation times of **1** could be obtained by fitting them to a QTM-only process to the following equation (1):

$$\tau^{-1} = \frac{B_1}{1+B_2H^2} \quad (1)$$

The best-fit parameters were: B_1 = (2.25 ± 0.83) x 10^{-1} s and B_2 = (1.06 ± 0.11) x 10^{-7} Oe^{-2}. Efforts to include a term accounting for the presence of a Raman process did not provide reasonable parameters (n ≤ 0) and was therefore excluded.

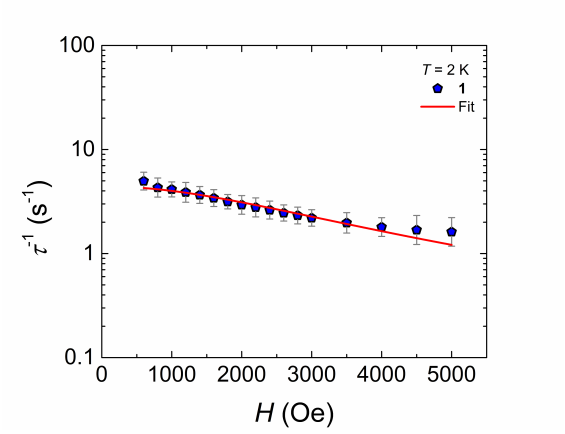

Fig. S18. Field-dependence of the relaxation times (τ) for compound **1** collected at 2 K with the respective estimated standard deviations (grey bars). These estimated standard deviations of the relaxation times have been calculated from the α-parameters of the generalized Debye fits with the log-normal distribution.[38] The solid red line represents the fit to eq.(1).

Given that no optimal field could be selected to probe the slow relaxation of the magnetization due to the absence of a maximum of the τ even at high fields, we selected to explore the ac susceptibility of **1** at 1400 Oe. This field is consistent with the magnetic studies of the ac susceptibility performed for the Tb(III) (**2**) and Dy(III) (**3**) analogues. As such, ac measurements were performed for **1** between 1.9 and 4 K under an applied static dc field of 1400 Oe, to investigate the temperature-dependence of the ac susceptibility at this field (Fig. S19). Indeed, in this temperature range, a temperature-independent signal was observed in the LF region, while tails of the susceptibility were observed in the HF region indicating the presence of a second process. As previously, the sum of two generalized Debye equations was employed to accurately fit the χ' and χ'' susceptibilities and extract the relaxation times. Reliable fitting parameters could only be

obtained for the LF process, because the presence of the HF process is only denoted by the tails of the ac susceptibility and no peak of the χ'' is observed in this frequency window.

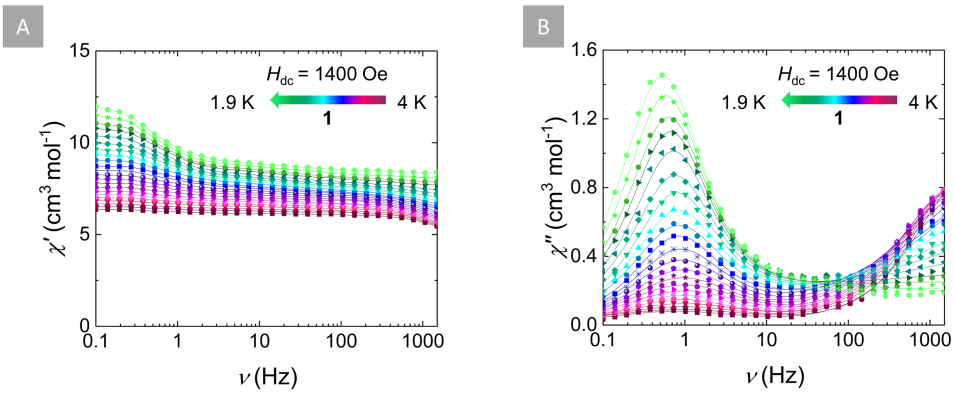

Fig. S19. The in-phase (χ') (A) and out-of-phase (χ'') (B) magnetic susceptibility of **1** at 1400 Oe, at the indicated temperature region. The solid lines represent the best-fit to the generalized Debye model.

Table S18. Fitting parameters obtained for the LF process using the sum of two generalized Debye equations for the ac data of **1** in the presence of a static dc field (H_{dc} = 1400 Oe) in the temperature region of 1.9 to 4 K (Fig. S19).

T (K)	τ (s)	α	χ_s (cm^3 mol^{-1})	χ_t (cm^3 mol^{-1})
1.9	3.00 x 10^{-1}	1.88 x 10^{-2}	5.52	8.29
2	2.78 x 10^{-1}	1.74 x 10^{-2}	5.90	8.33
2.1	2.55 x 10^{-1}	1.80 x 10^{-2}	5.81	7.99
2.2	2.42 x 10^{-1}	2.25 x 10^{-2}	6.13	8.10
2.3	2.24 x 10^{-1}	2.95 x 10^{-2}	6.03	7.79
2.4	2.15 x 10^{-1}	3.15 x 10^{-2}	6.31	7.92
2.5	2.05 x 10^{-1}	3.81 x 10^{-2}	6.18	7.63
2.6	1.99 x 10^{-1}	5.38 x 10^{-2}	6.47	7.76
2.7	1.95 x 10^{-1}	1.01 x 10^{-1}	6.27	7.54
2.8	1.96 x 10^{-1}	5.33 x 10^{-2}	6.61	7.62
2.9	1.88 x 10^{-1}	9.50 x 10^{-2}	6.43	7.38
3	1.82 x 10^{-1}	1.40 x 10^{-1}	6.61	7.50
3.1	1.76 x 10^{-1}	1.63 x 10^{-1}	6.51	7.30
3.2	1.76 x 10^{-1}	1.90 x 10^{-1}	6.58	7.30
3.3	1.66 x 10^{-1}	2.45 x 10^{-1}	6.57	7.24
3.4	1.64 x 10^{-1}	2.63 x 10^{-1}	6.61	7.20
3.5	1.74 x 10^{-1}	2.65 x 10^{-2}	6.65	7.17
3.6	1.85 x 10^{-1}	2.49 x 10^{-2}	6.69	7.12
3.7	1.75 x 10^{-1}	3.21 x 10^{-2}	6.70	7.11
3.8	1.82 x 10^{-1}	3.26 x 10^{-2}	6.73	7.09
3.9	1.85 x 10^{-1}	3.93 x 10^{-2}	6.74	7.08
4	2.14 x 10^{-1}	3.13 x 10^{-2}	6.77	7.04

As seen in Fig. S20, the extracted relaxation times for the LF process are temperature-independent, which is expected given the overlap of the χ'' peak in the LF region, indicative of the presence of QTM. Therefore, the extracted τ for this LF process can be fitted to a QTM-only term:

$$\tau^{-1} = \tau^{-1}_{QTM} \quad (2)$$

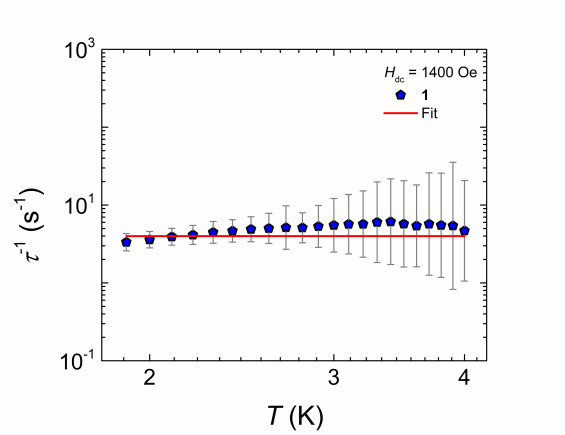

Fig. S20. Temperature-dependence of the relaxation times of the magnetization (τ^{-1}) at 1400 Oe with the respective estimated standard deviations (grey bars). These estimated standard deviations of the relaxation times have been calculated from the α-parameters of the generalized Debye fits with the log-normal distribution.[38] The solid red lines represent the best fit based on eq. (2).

The best-fit parameters for both the field and temperature-dependent τ can be found in Table S19.

Table S19. Best-fit parameters of the field-dependent and temperature-dependent relaxation times of the magnetization for **1**.

		1	
		Field-dependent	*Temperature-dependent* H_{dc} = 1400 Oe
QTM	B_1 (s)	(2.25 ± 0.83) x 10^{-1}	
	B_2 (Oe^{-2})	(1.06 ± 0.11) x 10^{-7}	
	τ_{QTM} (s)		(2.51 ± 0.08) x 10^{-1}

Ac Magnetism Plots for Complexes 2 and 3:

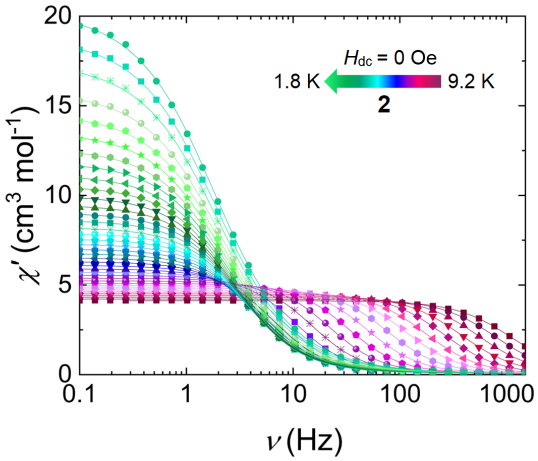

Fig. S21. Frequency-dependence of χ' as a function of temperature in the 9.2 to 1.8 K temperature range, in the absence of an applied field (H_{dc} = 0 Oe) for **2**. Solid lines represent best fits to the generalized Debye model.

Table S20. Fitting parameters obtained from CCFit-2[38] using a generalized Debye model for the ac data of **2** in the absence of a static dc field (H_{dc} = 0 Oe) in the temperature region of 1.8 to 9.2 K (Fig. 5A, 5B, S21).

T (K)	τ (s)	α	χ_s (cm^3 mol^{-1})	χ_t (cm^3 mol^{-1})
1.8	8.79 x 10^{-2}	2.20 x 10^{-1}	2.36 x 10^{-2}	20.4
2	8.56 x 10^{-2}	2.14 x 10^{-1}	3.81 x 10^{-2}	18.9
2.2	8.28 x 10^{-2}	2.07 x 10^{-1}	4.39 x 10^{-2}	17.5
2.4	7.88 x 10^{-2}	1.97 x 10^{-1}	5.28 x 10^{-2}	15.9
2.6	7.54 x 10^{-2}	1.88 x 10^{-1}	5.93 x 10^{-2}	14.6
2.8	7.21 x 10^{-2}	1.80 x 10^{-1}	6.28 x 10^{-2}	13.6
3	6.88 x 10^{-2}	1.72 x 10^{-1}	6.75 x 10^{-2}	12.7
3.2	6.58 x 10^{-2}	1.63 x 10^{-1}	6.88 x 10^{-2}	11.9
3.4	6.27 x 10^{-2}	1.54 x 10^{-1}	7.69 x 10^{-2}	11.2
3.6	5.98 x 10^{-2}	1.46 x 10^{-1}	7.70 x 10^{-2}	10.6
3.8	5.69 x 10^{-2}	1.38 x 10^{-1}	7.90 x 10^{-2}	10.0
4	5.40 x 10^{-2}	1.30 x 10^{-1}	8.18 x 10^{-2}	9.49
4.2	5.13 x 10^{-2}	1.23 x 10^{-1}	7.81 x 10^{-2}	9.04
4.4	4.88 x 10^{-2}	1.15 x 10^{-1}	8.24 x 10^{-2}	8.63
4.6	4.62 x 10^{-2}	1.08 x 10^{-1}	8.26 x 10^{-2}	8.22
4.8	4.41 x 10^{-2}	1.03 x 10^{-1}	8.02 x 10^{-2}	7.90
5	4.20 x 10^{-2}	9.73 x 10^{-2}	8.19 x 10^{-2}	7.58
5.2	4.00 x 10^{-2}	9.27 x 10^{-2}	8.26 x 10^{-2}	7.29
5.4	3.81 x 10^{-2}	8.79 x 10^{-2}	8.44 x 10^{-2}	7.02
5.6	3.62 x 10^{-2}	8.32 x 10^{-2}	8.52 x 10^{-2}	6.76
5.8	3.40 x 10^{-2}	7.86 x 10^{-2}	8.53 x 10^{-2}	6.53
6	3.14 x 10^{-2}	7.38 x 10^{-2}	8.38 x 10^{-2}	6.31
6.2	2.81 x 10^{-2}	6.76 x 10^{-2}	8.55 x 10^{-2}	6.10
6.4	2.41 x 10^{-2}	6.14 x 10^{-2}	8.22 x 10^{-2}	5.90
6.6	1.94 x 10^{-2}	5.61 x 10^{-2}	7.72 x 10^{-2}	5.72
6.8	1.47 x 10^{-2}	5.29 x 10^{-2}	7.33 x 10^{-2}	5.54
7	1.06 x 10^{-2}	5.30 x 10^{-2}	6.28 x 10^{-2}	5.38
7.2	7.26 x 10^{-3}	5.52 x 10^{-2}	5.52 x 10^{-2}	5.23
7.4	4.87 x 10^{-3}	5.81 x 10^{-2}	4.80 x 10^{-2}	5.09
7.6	3.20 x 10^{-3}	6.18 x 10^{-2}	3.52 x 10^{-2}	4.96
7.8	2.10 x 10^{-3}	6.53 x 10^{-2}	2.93 x 10^{-2}	4.84
8	1.39 x 10^{-3}	6.97 x 10^{-2}	1.37 x 10^{-2}	4.72
8.2	9.18 x 10^{-4}	7.34 x 10^{-2}	3.30 x 10^{-17}	4.61
8.4	6.18 x 10^{-4}	7.51 x 10^{-2}	3.48 x 10^{-21}	4.51
8.6	4.22 x 10^{-4}	7.82 x 10^{-2}	2.81 x 10^{-22}	4.41
8.8	2.91 x 10^{-4}	8.04 x 10^{-2}	1.95 x 10^{-20}	4.31
9	2.02 x 10^{-4}	8.21 x 10^{-2}	5.68 x 10^{-24}	4.22
9.2	1.42 x 10^{-4}	8.60 x 10^{-2}	5.13 x 10^{-21}	4.13

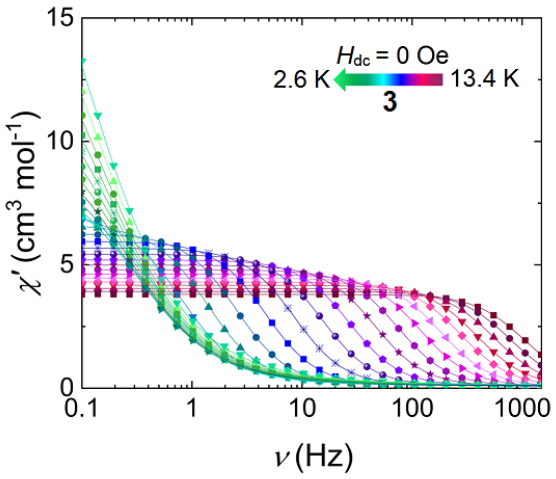

Fig. S22. Frequency-dependence of χ' as a function of temperature in the 13.4 to 2.6 K temperature range, in the absence of an applied field (H_{dc} = 0 Oe) for **3**. Solid lines represent best fits to the generalized Debye model.

Table S21. Fitting parameters obtained from CCFit-2[38] using a generalized Debye model for the ac data of **3** in the absence of a static dc field (H_{dc} = 0 Oe) in the temperature region of 2.6 to 13.4 K (Fig. 5E, 5F, S22).

T (K)	τ (s)	α	χ_s (cm^3 mol^{-1})	χ_t (cm^3 mol^{-1})
2.6	1.41	2.77 x 10^{-1}	1.49 x 10^{-1}	24.4
3	1.20	2.70 x 10^{-1}	1.47 x 10^{-1}	20.6
3.4	1.04	2.64 x 10^{-1}	1.45 x 10^{-1}	17.8
3.8	9.16 x 10^{-1}	2.58 x 10^{-1}	1.41 x 10^{-1}	15.6
4.2	8.12 x 10^{-1}	2.51 x 10^{-1}	1.40 x 10^{-1}	14.0
4.6	7.31 x 10^{-1}	2.45 x 10^{-1}	1.39 x 10^{-1}	12.6
5	6.69 x 10^{-1}	2.41 x 10^{-1}	1.34 x 10^{-1}	11.5
5.4	6.15 x 10^{-1}	2.37 x 10^{-1}	1.31 x 10^{-1}	10.6
5.8	5.70 x 10^{-1}	2.32 x 10^{-1}	1.29 x 10^{-1}	9.77
6.2	5.17 x 10^{-1}	2.21 x 10^{-1}	1.31 x 10^{-1}	9.08
6.6	4.35 x 10^{-1}	1.95 x 10^{-1}	1.36 x 10^{-1}	8.42
7	3.15 x 10^{-1}	1.47 x 10^{-1}	1.44 x 10^{-1}	7.72
74	2.00 x 10^{-1}	9.15 x 10^{-2}	1.45 x 10^{-1}	7.12
7.8	1.15 x 10^{-1}	5.50 x 10^{-2}	1.32 x 10^{-1}	6.64
8.2	6.33 x 10^{-2}	3.58 x 10^{-2}	1.18 x 10^{-1}	6.27
8.6	3.43 x 10^{-2}	2.72 x 10^{-2}	1.05 x 10^{-1}	5.95
9	1.87 x 10^{-2}	2.42 x 10^{-2}	9.48 x 10^{-2}	5.68
9.4	1.04 x 10^{-2}	2.37 x 10^{-2}	8.62 x 10^{-2}	5.43
9.8	5.89 x 10^{-3}	2.38 x 10^{-2}	8.04 x 10^{-2}	5.20
10.2	3.47 x 10^{-3}	2.33 x 10^{-2}	7.66 x 10^{-2}	4.99
10.6	2.12 x 10^{-3}	2.28 x 10^{-2}	7.21 x 10^{-2}	4.80
11	1.33 x 10^{-3}	2.30 x 10^{-2}	6.65 x 10^{-2}	4.62
11.4	8.64 x 10^{-4}	2.35 x 10^{-2}	5.94 x 10^{-2}	4.46
11.8	5.76 x 10^{-4}	2.54 x 10^{-2}	5.52 x 10^{-2}	4.30
12.2	4.08 x 10^{-4}	2.41 x 10^{-2}	5.40 x 10^{-2}	4.18
12.6	2.85 x 10^{-4}	2.43 x 10^{-2}	4.60 x 10^{-2}	4.04
13	2.04 x 10^{-4}	2.59 x 10^{-2}	4.29 x 10^{-2}	3.92
13.4	1.49 x 10^{-4}	2.53 x 10^{-2}	4.43 x 10^{-2}	3.80

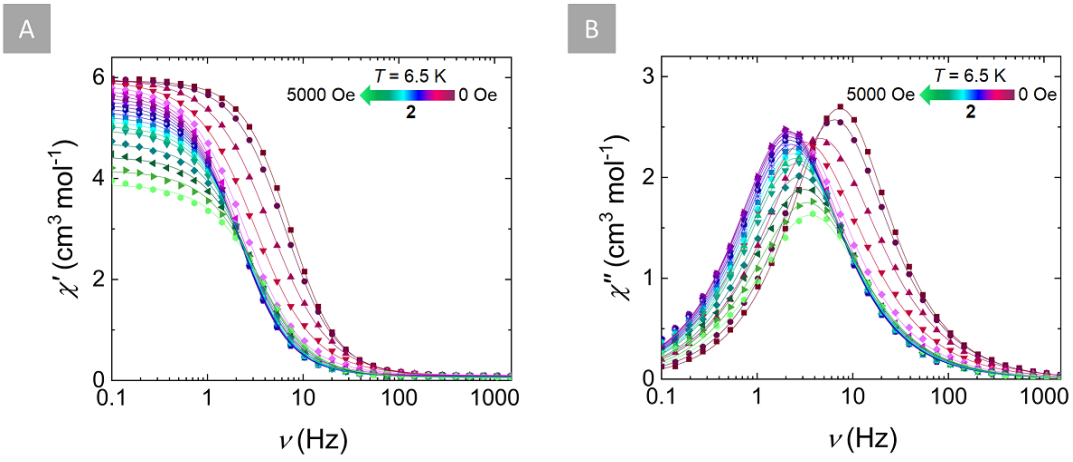

Fig. S23. Field-dependence of the χ' (A) and χ'' (B) magnetic susceptibility of **2** at 6.5 K in the field range of 0 to 5000 Oe. For the χ' the solid lines serve as a guide to the eye, while for the χ'' the solid lines represent the best fit to the generalized Debye model.

Table S22. Best-fit parameters to the generalized Debye model for the frequency dependence of the out-of-phase-magnetic susceptibility (χ'') as a function of field for **2** collected at T = 6.5 K (Fig. S23).

H (Oe)	τ (s)	α	χ_s (cm^3 mol^{-1})	χ_t (cm^3 mol^{-1})
0	2.18 x 10^{-1}	5.53 x 10^{-2}	8.22 x 10^{-2}	5.94
200	2.46 x 10^{-2}	8.37 x 10^{-2}	7.57 x 10^{-2}	5.95
400	3.50 x 10^{-2}	1.37 x 10^{-1}	6.70 x 10^{-2}	6.01
600	5.05 x 10^{-2}	14.1 x 10^{-1}	8.84 x 10^{-2}	5.97
800	6.41 x 10^{-2}	1.17 x 10^{-1}	9.78 x 10^{-2}	5.88
1000	7.19 x 10^{-2}	9.56 x 10^{-2}	9.59 x 10^{-2}	5.78
1200	7.49 x 10^{-2}	8.37 x 10^{-2}	8.84 x 10^{-2}	5.72
1400	7.56 x 10^{-2}	7.79 x 10^{-2}	8.18 x 10^{-2}	5.63
1600	7.50 x 10^{-2}	7.52 x 10^{-2}	7.81 x 10^{-2}	5.56
1800	7.37 x 10^{-2}	7.50 x 10^{-2}	7.25 x 10^{-2}	5.49
2000	7.19 x 10^{-2}	7.67 x 10^{-2}	6.73 x 10^{-2}	5.41
2200	7.00 x 10^{-2}	7.83 x 10^{-2}	6.32 x 10^{-2}	5.33
2400	6.80 x 10^{-2}	7.95 x 10^{-2}	6.54 x 10^{-2}	5.25
2600	6.59 x 10^{-2}	8.22 x 10^{-2}	6.39 x 10^{-2}	5.16
2800	6.37 x 10^{-2}	8.43 x 10^{-2}	6.23 x 10^{-2}	5.06
3000	6.15 x 10^{-2}	8.82 x 10^{-2}	5.52 x 10^{-2}	4.97
3500	5.64 x 10^{-2}	9.37 x 10^{-2}	4.89 x 10^{-2}	4.71
4000	5.16 x 10^{-2}	9.93 x 10^{-2}	4.69 x 10^{-2}	4.45
4500	4.75 x 10^{-2}	1.03 x 10^{-1}	4.53 x 10^{-2}	4.17
5000	4.41 x 10^{-2}	1.06 x 10^{-1}	4.91 x 10^{-2}	3.90

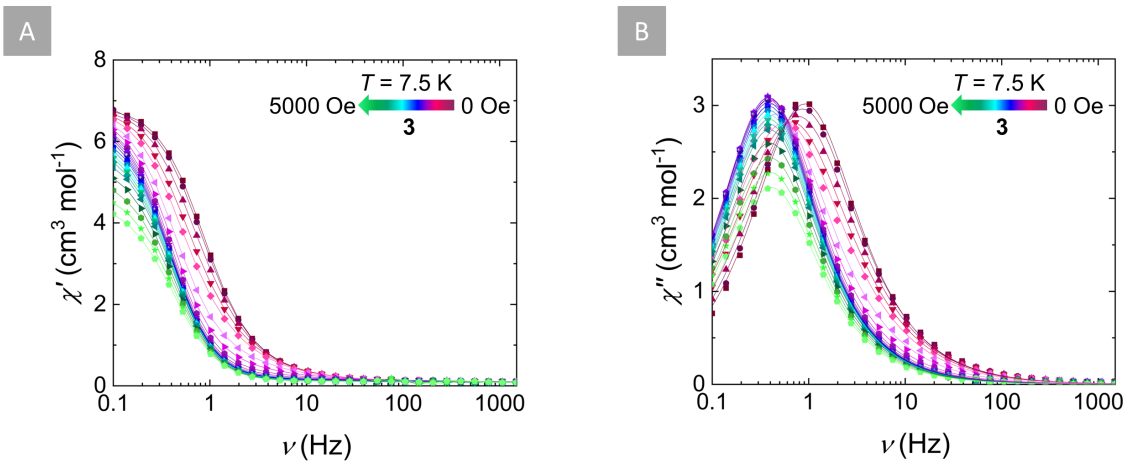

Fig. S24. Field-dependence of the χ' (A) and χ'' (B) magnetic susceptibility of **3** at 7.5 K in the field range of 0 to 5000 Oe. For the χ' the solid lines serve as a guide to the eye, while for the χ'' the solid lines represent the best fit to the generalized Debye model.

Table S23. Best-fit parameters to the generalized Debye model for the frequency dependence of the out-of-phase-magnetic susceptibility (χ'') as a function of field for **3** collected at T = 7.5 K (Fig. S24).

H (Oe)	τ (s)	α	χ_s (cm^3 mol^{-1})	χ_t (cm^3 mol^{-1})
0	1.74 x 10^{-1}	7.90 x 10^{-2}	1.45 x 10^{-1}	6.98
100	1.85 x 10^{-1}	9.85 x 10^{-2}	1.34 x 10^{-1}	7.06
200	2.06 x 10^{-1}	1.15 x 10^{-2}	1.35 x 10^{-1}	7.06
300	2.41 x 10^{-1}	1.33 x 10^{-2}	1.36 x 10^{-1}	7.11
400	2.80 x 10^{-1}	1.36 x 10^{-2}	1.42 x 10^{-1}	7.14
600	3.47 x 10^{-1}	1.08 x 10^{-2}	1.58 x 10^{-1}	7.06
800	3.87 x 10^{-1}	7.18 x 10^{-2}	1.57 x 10^{-1}	6.91
1000	4.06 x 10^{-1}	4.91 x 10^{-2}	1.42 x 10^{-1}	6.77
1200	4.14 x 10^{-1}	3.74 x 10^{-2}	1.33 x 10^{-1}	6.68
1400	4.17 x 10^{-1}	3.12 x 10^{-2}	1.25 x 10^{-1}	6.60
1600	4.17 x 10^{-1}	2.72 x 10^{-2}	1.20 x 10^{-1}	6.52
1800	4.16 x 10^{-1}	2.47 x 10^{-2}	1.18 x 10^{-1}	6.42
2000	4.13 x 10^{-1}	2.34 x 10^{-2}	1.13 x 10^{-1}	6.33
2200	4.12 x 10^{-1}	2.28 x 10^{-2}	1.12 x 10^{-1}	6.23
2400	4.10 x 10^{-1}	2.16 x 10^{-2}	1.10 x 10^{-1}	6.11
2600	4.09 x 10^{-1}	2.29 x 10^{-2}	1.05 x 10^{-1}	6.02
2800	4.06 x 10^{-1}	2.18 x 10^{-2}	1.06 x 10^{-1}	5.90
3000	4.05 x 10^{-1}	2.34 x 10^{-2}	1.00 x 10^{-1}	5.79
3500	4.03 x 10^{-1}	2.39 x 10^{-2}	0.96 x 10^{-1}	5.49
4000	4.00 x 10^{-1}	2.50 x 10^{-2}	1.01 x 10^{-1}	5.17
4500	3.98 x 10^{-1}	2.60 x 10^{-2}	1.02 x 10^{-1}	4.85
5000	3.92 x 10^{-1}	2.86 x 10^{-2}	1.00 x 10^{-1}	4.53

Fit of the field-dependent relaxation times for 2 and 3:

To further investigate the relaxation dynamics in **2** and **3** the extracted relaxation times from the field-dependent ac susceptibility (χ' and χ'') can be fit to the following equation:

$$\tau^{-1} = \tau_{QTM}^{-1} + \tau_{Raman}^{-1} + \tau_{Direct}^{-1} + \tau_{Orbach}^{-1}$$

$$\tau^{-1} = \frac{B_1}{1+B_2H^2} + \frac{1+C_1H^2}{1+C_2H^2}CT^n + ATH^m + \tau_0^{-1}\exp\left(\frac{-U_{eff}}{k_BT}\right) \quad (3)$$

For **2**, the inclusion of all four relaxation mechanisms yielded a satisfactory fit as can be seen in Fig. S25. In order to achieve that, m was set to be equal to 2, as is for non-Kramers ions and the terms C1 and C2 were fixed to be zero as the fit could not provide any meaningful values for these parameters. For **3**, the inclusion of all four relaxation mechanisms did not provide a satisfactory fit and therefore some simplifications of this equation had to be taken into account. Given the field-independence of the τ at fields higher than 1400 Oe, it is obvious that temperature-dependent mechanisms drive the relaxation of the magnetization at higher fields. As such, the direct term, which is clearly a field-dependent contribution, can be exempt from the fit. Regarding the Raman contribution, although attempts to include it in the fit were made, no reliable parameters could be obtained and it was therefore exempt from the fit. As such, for **3**, the field-dependent relaxation times were fit to a combination of QTM and Orbach processes according to equation (4):

$$\tau^{-1} = \tau_{QTM}^{-1} + \tau_{Orbach}^{-1}$$

$$\tau^{-1} = \frac{B_1}{1+B_2H^2} + \tau_0^{-1}\exp\left(\frac{-U_{eff}}{k_BT}\right) \quad (4)$$

Indeed, as can be seen in Fig. S26, a satisfactory fit can be obtained for a combination of QTM and Orbach processes. The best-fit parameters for the field-dependent τ for both **2** and **3** are in good agreement with the best-fit parameters of the temperature-dependent τ and can be found in Table S24.

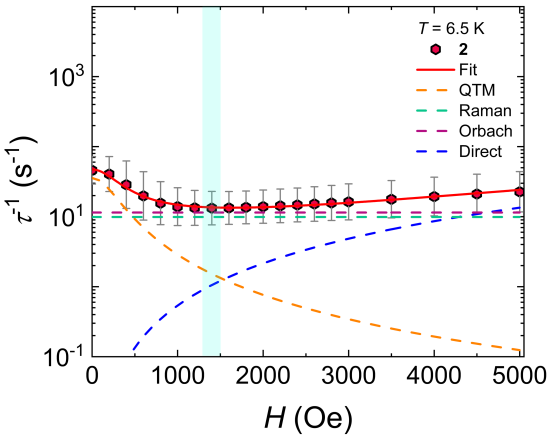

Fig. S25. Field-dependence of the relaxation times (τ^{-1}) for **2** at a fixed temperature of 6.5 K with the respective estimated standard deviations (gray bars). These estimated standard deviations of the relaxation times have been calculated from the α-parameters of the generalized Debye fits with the log-normal distribution.[38] The relaxation times were obtained from the generalized Debye model (Table S22). The optimal static field for which the relaxation times are longest and quantum tunneling of the magnetization is suppressed, is highlighted with a light-green line. This is the field at which temperature-dependent relaxation studies under a static dc field were conducted at (*vide infra*). The solid red line represents the fit to eq(3), while the dashed orange, teal, purple and blue lines represent the individual components of the magnetic relaxation for QTM, Raman, Orbach and direct processes, respectively.

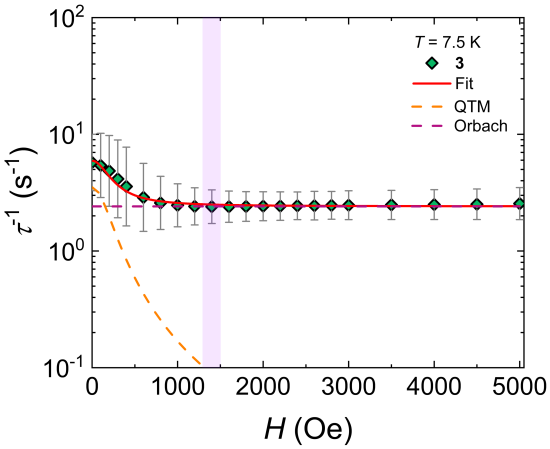

Fig. S26. Field-dependence of the relaxation times (τ^{-1}) for **3** at a fixed temperature of 7.5 K with the respective estimated standard deviations (gray bars). These estimated standard deviations of the relaxation times have been calculated from the α-parameters of the generalized Debye fits with the log-normal distribution.[38] The relaxation times were obtained from the generalized Debye model (Table S23). The optimal static field for which the relaxation times are longest and quantum tunneling of the magnetization is suppressed, is highlighted with a light-purple line. This is the field at which temperature-dependent relaxation studies under a static dc field were conducted at (*vide infra*). The solid red line represents the fit to eq(4), while the dashed orange and purple lines represent the individual components of the magnetic relaxation for QTM and Orbach processes, respectively.

Table S24. Best-fit parameters of the field-dependent relaxation times of the magnetization for **2** and **3**.

		2	3
QTM	B_1 (s)	(2.81 ± 0.10) x 10^{-2}	(2.84 ± 0.24) x 10^{-1}
	B_2 (Oe^{-2})	(1.14 ± 0.18) x 10^{-5}	(1.99 ± 0.55) x 10^{-5}
Raman	C (s^{-1} K^{-n})	0.20 ± 0.05	
	n	2.09 ± 0.04	
Orbach	τ_0 (s)	(5.77 ± 0.26) x 10^{-11}	(8.38 ± 0.38) x 10^{-8}
	U_{eff} (cm^{-1})	99.8 ± 6.85	88.8 ± 4.03
Direct	A (K^{-1} Oe^{-4} s^{-1})	(8.29 ± 0.63) x 10^{-8}	

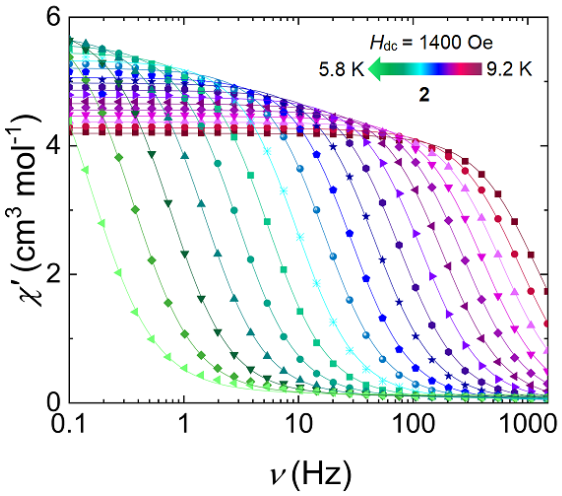

Fig. S27. Frequency-dependence of χ' as a function of temperature in the 9.2 to 5.8 K temperature range, under an applied static field of 1400 Oe for **2**. Solid lines represent best fits to the generalized Debye model.

Table S25. Fitting parameters obtained from CCFit-2[38] using a generalized Debye model for the ac data of **2** in the presence of a static dc field (H_{dc} = 1400 Oe) in the temperature region of 5.8 to 9.2 K (Fig. 5C, 5D, S27).

T (K)	τ (s)	α	χ_S (cm^3 mol^{-1})	χ_t (cm^3 mol^{-1})
5.8	1.02	1.06 x 10^{-1}	1.32 x 10^{-1}	6.47
6	4.41 x 10^{-1}	8.67 x 10^{-2}	1.17 x 10^{-1}	6.09
6.2	2.09 x 10^{-1}	8.05 x 10^{-2}	1.01 x 10^{-1}	5.89
6.4	1.05 x 10^{-1}	7.77 x 10^{-2}	8.89 x 10^{-2}	5.73
6.6	5.46 x 10^{-2}	7.66 x 10^{-2}	7.56 x 10^{-2}	5.59
6.8	2.95 x 10^{-2}	7.64 x 10^{-2}	6.45 x 10^{-2}	5.46
7	1.65 x 10^{-2}	7.57 x 10^{-2}	5.73 x 10^{-2}	5.33
7.2	9.45 x 10^{-3}	7.69 x 10^{-2}	4.24 x 10^{-2}	5.21
7.4	5.56 x 10^{-3}	7.31 x 10^{-2}	3.53 x 10^{-2}	5.06
7.6	3.41 x 10^{-3}	7.95 x 10^{-2}	2.64 x 10^{-2}	4.98
7.8	2.12 x 10^{-3}	8.06 x 10^{-2}	1.48 x 10^{-2}	4.87
8	1.35 x 10^{-3}	8.25 x 10^{-2}	7.47 x 10^{-3}	4.76
8.2	8.79 x 10^{-4}	8.51 x 10^{-2}	6.27 x 10^{-19}	4.66
8.4	5.83 x 10^{-4}	8.65 x 10^{-2}	5.26 x 10^{-18}	4.56
8.6	3.94 x 10^{-4}	8.87 x 10^{-2}	3.60 x 10^{-20}	4.46
8.8	2.70 x 10^{-4}	9.14 x 10^{-2}	1.86 x 10^{-20}	4.37
9	1.87 x 10^{-4}	9.29 x 10^{-2}	3.66 x 10^{-22}	4.28
9.2	1.32 x 10^{-4}	9.59 x 10^{-2}	1.57 x 10^{-21}	4.19

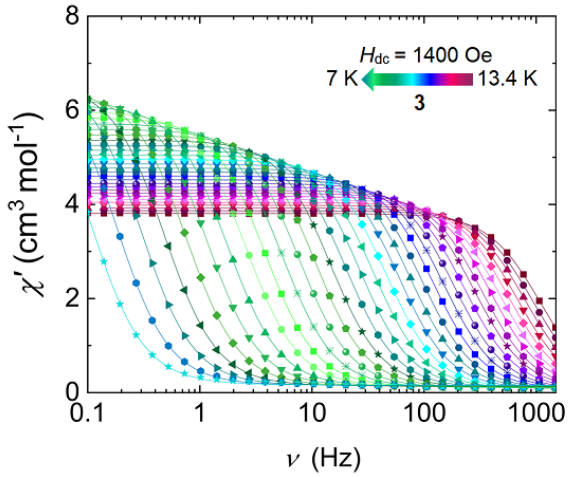

Fig. S28. Frequency-dependence of χ' as a function of temperature in the 13.4 to 7 K temperature range, under an applied static field of 1400 Oe for **3**. Solid lines represent best fits to the generalized Debye model.

Table S26. Fitting parameters obtained from CCFit-2[38] using a generalized Debye model for the ac data of **3** in the presence of a static dc field (H_{dc} = 1400 Oe) in the temperature region of 7 to 13.4 K (Fig. 5G, 5H, S28).

T (K)	τ (s)	α	χ_s (cm^3 mol^{-1})	χ_t (cm^3 mol^{-1})
7	1.54	4.26 x 10^{-2}	1.59 x 10^{-1}	7.24
7.2	8.88 x 10^{-1}	3.42 x 10^{-2}	1.56 x 10^{-1}	6.95
7.4	5.35 x 10^{-1}	3.26 x 10^{-2}	1.48 x 10^{-1}	6.76
7.6	3.31 x 10^{-1}	3.22 x 10^{-2}	1.39 x 10^{-1}	6.58
7.8	2.10 x 10^{-1}	3.12 x 10^{-2}	1.36 x 10^{-1}	6.42
8	1.36 x 10^{-1}	3.07 x 10^{-2}	1.28 x 10^{-1}	6.27
8.2	9.02 x 10^{-2}	2.95 x 10^{-2}	1.24 x 10^{-1}	6.12
8.4	6.09 x 10^{-2}	2.93 x 10^{-2}	1.18 x 10^{-1}	5.98
8.6	4.20 x 10^{-2}	2.80 x 10^{-2}	1.15 x 10^{-1}	5.85
8.8	2.93 x 10^{-2}	2.73 x 10^{-2}	1.05 x 10^{-1}	5.72
9	2.08 x 10^{-2}	2.66 x 10^{-2}	1.02 x 10^{-1}	5.60
9.2	1.50 x 10^{-2}	2.59 x 10^{-2}	1.01 x 10^{-1}	5.48
9.4	1.09 x 10^{-2}	2.53 x 10^{-2}	9.62 x 10^{-2}	5.37
9.6	8.02 x 10^{-3}	2.54 x 10^{-2}	9.19 x 10^{-2}	5.26
9.8	6.00 x 10^{-3}	2.44 x 10^{-2}	8.81 x 10^{-2}	5.15
10	4.53 x 10^{-3}	2.41 x 10^{-2}	8.69 x 10^{-2}	5.05
10.2	3.47 x 10^{-3}	2.44 x 10^{-2}	8.26 x 10^{-2}	4.95
10.4	2.69 x 10^{-3}	2.26 x 10^{-2}	8.12 x 10^{-2}	4.86
10.6	2.10 x 10^{-3}	2.39 x 10^{-2}	7.92 x 10^{-2}	4.77
10.8	1.66 x 10^{-3}	2.34 x 10^{-2}	7.39 x 10^{-2}	4.69
11	1.32 x 10^{-3}	2.21 x 10^{-2}	7.32 x 10^{-2}	4.60
11.2	1.06 x 10^{-3}	2.33 x 10^{-2}	7.14 x 10^{-2}	4.52
11.4	8.55 x 10^{-4}	2.35 x 10^{-2}	6.66 x 10^{-2}	4.45
11.6	6.96 x 10^{-4}	2.41 x 10^{-2}	6.67 x 10^{-2}	4.37
11.8	5.70 x 10^{-4}	2.51 x 10^{-2}	6.38 x 10^{-2}	4.30
12	4.84 x 10^{-4}	2.45 x 10^{-2}	6.26 x 10^{-2}	4.24
12.2	4.02 x 10^{-4}	2.57 x 10^{-2}	5.74 x 10^{-2}	4.17
12.4	3.35 x 10^{-4}	2.63 x 10^{-2}	4.83 x 10^{-2}	4.11
12.6	2.82 x 10^{-4}	2.78 x 10^{-2}	4.31 x 10^{-2}	4.04
12.8	2.38 x 10^{-4}	2.82 x 10^{-2}	4.13 x 10^{-2}	3.98
13	2.02 x 10^{-4}	2.95 x 10^{-2}	3.89 x 10^{-2}	3.92
13.2	1.72 x 10^{-4}	2.69 x 10^{-2}	4.72 x 10^{-2}	3.86
13.4	1.46 x 10^{-4}	2.96 x 10^{-2}	3.07 x 10^{-2}	3.81

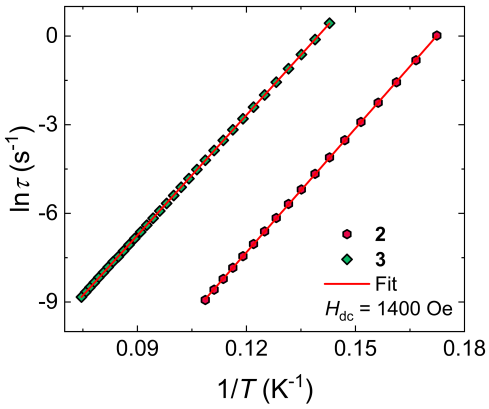

Fig. S29. Arrhenius plot of the natural log of the relaxation time, τ, of the magnetization for **2** (magenta hexagons) and **3** (teal diamonds) versus the inverse temperature. The red line represents the linear fit to the Arrhenius equation that affords a U_{eff} = 97.2 cm^{-1} for **2** and U_{eff} = 94.2 cm^{-1} for **3**.

Table S27. Best-fit parameters of the temperature-dependent relaxation times of the magnetization for **2** and **3**, in the absence and presence of a dc field (1400 Oe).

		2		**3**	
		H_{dc} = 0 Oe	H_{dc} = 1400 Oe	H_{dc} = 0 Oe	H_{dc} = 1400 Oe
QTM	τ_{QTM} (s)	(1.04 ± 0.03) x 10^{-1}		(6.88 ± 0.77) x 10^{-1}	
Raman	C (s^{-1} K^{-n})	0.49 ± 0.06			
	n	2.09 ± 0.06			
Orbach	τ_0 (s)	(3.34 ± 0.20) x 10^{-11}	(3.43 ± 0.10) x 10^{-11}	(1.00 ± 0.10) x 10^{-8}	(6.04 ± 0.05) x 10^{-9}
	U_{eff} (cm^{-1})	97.8 ± 13.4	97.2 ± 5.09	90.2 ± 3.79	94.1 ± 2.00

8. References

[1] M. D. Coburn, G. A. Buntain, B. W. Harris, M. A. Hiskey, K.-Y. Lee, D. G. Ott, *J. Heterocyclic Chem.*, 1991,**28**, 2049-2050.

[2] S. Demir, J. M. Zadrozny, M. Nippe and J. R. Long, *J. Am. Chem. Soc.*, 2012, **134**, 18546–18549.

[3] G. M. Sheldrick, SADABS, *Bruker/Siemens Area Detector Absorption Correction Program V.2.0.3*, Bruker AXS: Madison, WI, 2003.

[4] G. M. Sheldrick, *Acta Crystallogr. Sect. A: Found. Adv.*, 2015, A**71**, 3–8.

[5] G. M. Sheldrick, *SHELXL 2018/3: Programme for Crystal structure refinement, Acta Crystallogr. Sect. C.*, 2015, C**71**, 3–8.

[6] A. L. Spek, *Acta Crystallogr.*, 2015, C**71**, 9–18.

[7] A. L. Spek, *Acta Crystallogr.*, 1990, A**46**, C34.

[8] L. J. Farrugia, *J. Appl. Crystallogr.*, 1999, **32**, 837–838.

[9] K. Brandenburg, *DIAMOND: Program for Crystal and Molecular Structure Visualization*, Crystal Impact GbR, Bonn, Germany, 2014.

[10] C. F. Macrae, P. R. Edgington, P. McCabe, E. Pidcock, G. P. Shields, R. Taylor, M. Towler and J. van de Streek, *J. Appl. Crystallogr.*, 2006, **39**, 453–457.

[11] N. F. Chilton, R. P. Anderson, L. D. Turner, A. Soncini, K. S. Murray, *J. Comput. Chem.*, 2013, **34**, 1164-1175.

[12] J. van Tol, L.-C. Brunel, *Rev. Sci. Instrum.* 2005, **76**, 074101.

[13] G. W. Morley, L.-C. Brunel, J. van Tol, *Rev. Sci. Instrum.* 2008, **79**, 064703.

[14] S. Stoll, A. Schweiger, *J. Magn. Reson.* 2006, **178**, 42-55.

[15] J. Hrubý, V. T. Santana, D. Kostiuk, M. Bouček, S. Lenz, M. Kern, P. Šiffalovič, J. van Slageren, P. Neugebauer, *RSC Adv.* 2019, **9**, 24066-24073.

[16] M. A. Hay, A. Sarkar, G. A. Craig, L. Bhaskaran, J. Nehrkom, M. Ozerov, K. E. R. Marriott, C. Wilson, G. Rajaraman, S. Hill, M. Murrie, *Chem. Sci.* 2019, **10**, 6354-6361.

[17] M. K. Baker, S. J. Blundell, N. Domingo, S. Hill. *Spectroscopy Methods for Molecular Nanomagnets* in: *Molecular Nanomagnets and Related Phenomena. Structure and Bonding,* S. Gao (eds), Springer, Berlin, Heidelberg, vol 164 (2014), pp 231-291.

[18] S. Hill, S. Datta, J. Liu, R. Inglis, C. J. Milios, P. L. Feng, J. J. Henderson, E. del Barco, E. K. Brechin, D. K. Hendrickson, *Dalton Trans.* 2010, **39**, 4693-4707.

[19] a) B. O. Roos, P. R. Taylor, P. E. M. Sigbahn, *Chem. Phys.*, 1980, **48**, 157-173; b) B. O. Roos, R. Lindh, P. Å. Malmqvist, V. Veryazov, P.-O. Widmark, *Multiconfigurational quantum chemistry,* Wiley, 2016.

[20] I. F. Galván, M. Vacher, A. Alavi, C. Angeli, F. Aquilante, J. Autschbach, J. J. Bao, S. I. Bokarev, N. A. Bogdanov, R. K. Carlson, L. F. Chibotaru, J. Creutzberg, N. Dattani, M. G. Delcey, S. S. Dong, A. Dreuw, L. Freitag, L. M. Frutos, L. Gagliardi, F. Gendron, A. Giussani, L. González, G. Grell, M. Guo, C. E. Hoyer, M. Johansson, S. Keller, S. Knecht, G. Kovačević, E. Källman, G. Li Manni, M. Lundberg, Y. Ma, S. Mai, J. P. Malhado, P. Å. Malmqvist, P. Marquetand, S. A. Mewes, J. Norell, M. Olivucci, M. Oppel, Q. M. Phung, K. Pierloot, F. Plasser, M. Reiher, A. M. Sand, I. Schapiro, P. Sharma, C. J. Stein, L. Kragh Sørensen, D. G. Truhlar, M. Ugandi, L. Ungur, A. Valentini, S. Vancoillie, V. Veryazov, O. Weser, T. A. Wesołowski, P.-O. Widmark, S. Wouters, A. Zech,.J. P. Zobel, R. Lindh, *J. Chem. Theory Comput.*, 2019, **15**, 5925-5964.

[21] N. Mavragani, D. Errulat, D. A. Gálico, A. A. Kitos, A. Mansikkamäki, M. Murugesu, *Angew. Chem. Int. Ed.*, 2021, **60**, 24206-24213.

[22] P. Å. Malmqvist, B. O. Roos, B. Schimmelpfennig, *Chem. Phys. Lett.*, 2002, **357**, 230-240.

[23] a) W. Kutzalnigg, W. Liu, *J. Chem. Phys.*, 2005, **123**, 241102; b) D. Peng, M. Reiher, *Theor. Chem. Acc.*, 2012, **131**, 1081; c) M. Filatov, *J. Chem. Phys.*, 2006, **125**, 107101.

[24] a) B. O. Roos, R. Lindh, P. Å. Malmqvist, V. Veryazov, P.-O. Widmark, A. C. Borin, *J. Phys. Chem.*, 2008, **112**, 11431-11435; b) B. O. Roos, R. Lindh, P. Å. Malmqvist, V. Veryazov, P.-O. Widmark, *J. Phys. Chem. A*, 2004, **108**, 2851-2858.

[25] a) L. Ungur, L. F. Chibotaru, *Chem. Eur. J.*, 2017, **23**, 3708-3718; b) L. Ungur, M. Thewissen, J.-P. Costes, W. Wernsdorfer, L. F. Chibotaru, *Inorg. Chem.*, 2013, **52**, 6328-6337; c) L. F. Chibotaru, L. Ungur, *J. Chem. Phys.*, 2012, **137**, 064112.

[26] M. E. Lines, *J. Chem. Phys.*, 1971, **55**, 2977-2984.

[27] a) C. Lee, W. Yang, R. G. Parr, *Phys. Rev. B*, 1988, **37**, 785-789; b) A. D. Becke, *Phys. Rev. A*, 1988, **38**, 3098-3100; c) A. D. Becke, *J. Chem. Phys.*, 1993, **98**, 5648-5652.

[28] T. R. Cundari, W. J. Stevens, *J. Chem. Phys.*, 1993, **98**, 5555-5565.

[29] a) F. Weigend, R. Ahlrichs, *Phys. Chem. Chem. Phys.*, 2005, **7**, 3297-3305; b) B. P. Pritchard, D. Altarawy, B. Didier, T. D. Gibson, T. L. Windus, *J. Chem. Inf. Model.*, 2019, **59**, 4814-4820; c) D. Feller, *J. Comput. Chem.*, 1996, **17**, 1571-1586; d) K. L. Schuchardt, B. T. Didier, T. Elsethagen, L. Sun, V. Gurumoorthi, J. Chase, J. Lin, T. L. Windus, *J. Chem. Inf. Model.*, 2007, **47**, 1045-1052.

[30] a) S. Grimme, S. Ehrlich, L. Goerick, *J. Comput. Chem.*, 2011, **32**, 1456-1465; b) S. Grimme, J. Antony, S. Ehrlich, H. Krieg, *J. Chem. Phys.*, 2010, **132**, 154104.

[31] a) T. Yanai, D. P. Tew, N. C. Handy, *Chem. Phys. Lett.*, 2004, **393**, 51-57; b) D. A. Pantazis, F. Neese, *J. Chem. Theory Comput.*, 2009, **5**, 2229-2238; c) F. Weigend, *Phys. Chem. Chem. Phys.*, 2006, **8**, 1057-1065.

[32] C. van Wüllen, *J. Chem. Phys.*, 1998, **109**, 392-399.

[33] R. Maurice, C. de Graaf, N. Guihery, *Phys. Chem. Chem. Phys.*, 2013, **15**, 18784.

[34] a) N. Iwahara, L. F. Chibotaru, *Phys. Rev. B*, 2015, **91**, 174438; b) N. Iwahara, L. Ungur, L. F. Chibotaru, *Phys. Rev. B*, 2018, **98**, 054436.

[35] D. Andrae, U. Häußermann, M. Dolg, H. Stoll, H. Preuß, *Theor. Chim. Acta*, 1990, **77**, 123-141.

[36] Gaussian 16, Revision C.01, M. J. Frisch, G. W. Trucks, H. B. Schlegel, G. E. Scuseria, M. A. Robb, J. R. Cheeseman, G. Scalmani, V. Barone, G. A. Petersson, H. Nakatsuji, X. Li, M. Caricato, A. V. Marenich, J. Bloino, B. G. Janesko, R. Gomperts, B. Mennucci, H. P. Hratchian, J. V. Ortiz, A. F. Izmaylov, J. L. Sonnenberg, D. Williams-Young, F. Ding, F. Lipparini, F. Egidi, J. Goings, B. Peng, A. Petrone, T. Henderson, D. Ranasinghe, V. G. Zakrzewski, J. Gao, N. Rega, G. Zheng, W. Liang, M. Hada, M. Ehara, K. Toyota, R. Fukuda, J. Hasegawa, M. Ishida, T. Nakajima, Y. Honda, O. Kitao, H. Nakai, T. Vreven, K. Throssell, J. A. Montgomery, Jr., J. E. Peralta, F. Ogliaro, M. J. Bearpark, J. J. Heyd, E. N. Brothers, K. N. Kudin, V. N. Staroverov, T. A. Keith, R. Kobayashi, J. Normand, K. Raghavachari, A. P. Rendell, J. C. Burant, S. S. Iyengar, J. Tomasi, M. Cossi, J. M. Millam, M. Klene, C. Adamo, R. Cammi, J. W. Ochterski, R. L. Martin, K. Morokuma, O. Farkas, J. B. Foresman, and D. J. Fox, Gaussian, Inc., Wallingford CT, 2016.

[37] F. Neese, "The ORCA program system" *Wiley Interdisciplinary Reviews: Computational Molecular Science*, 2012, **2**, 73-78.

[38] D. Reta and N. F. Chilton, *Phys. Chem. Chem. Phys.* 2019, **21**, 23567-23575.